OXFORD

Journal of Petrology, 2023, **64**, 1–18
https://doi.org/10.1093/petrology/egad074
Advance access publication date 3 October 2023
Original Manuscript

The Influence of Undercooling and Sector Zoning on Clinopyroxene–Melt Equilibrium and Thermobarometry

Alice MacDonald [1,*], Teresa Ubide[1], Silvio Mollo [2,3], Alessio Pontesilli [3] and Matteo Masotta [4]

[1]School of the Environment, The University of Queensland, St. Lucia, Queensland, 4072, Australia
[2]Department of Earth Sciences, Sapienza-University of Rome, P. le Aldo Moro 5, 00185 Roma, Italy
[3]Istituto Nazionale di Geofisica e Vulcanologia, Sezione di Roma 1, Via di Vigna Murata 605, 00143 Roma, RM, Italy
[4]Dipartimento di Scienze della Terra, Università di Pisa, Via S. Maria 53, 56126 Pisa, Italy

*Corresponding author. E-mail: alice.macdonald@uq.edu.au

Abstract

Thermobarometry provides a critical means of assessing locations of magma storage and dynamics in the lead-up to volcanic eruptions and crustal growth. A common approach is to utilise minerals that have compositions sensitive to changes in pressure and/or temperature, such as clinopyroxene, which is ubiquitous in mafic to intermediate magmas. However, clinopyroxene thermobarometry may carry significant uncertainty and require an appropriate equilibrium melt composition. In addition, the degree of magma undercooling (ΔT) affects clinopyroxene composition and zoning, with common sector zoning potentially obfuscating thermobarometry results. Here, we use a set of crystallisation experiments on a primitive trachybasalt from Mt. Etna (Italy) at $\Delta T = 25$–233 °C, $P = 400$–800 MPa, $H_2O = 0$–4 wt % and $fO_2 = NNO + 2$, with clinopyroxene crystals defined by Al-rich zones (prisms and skeletons) and Al-poor zones (hourglass and overgrowths) to assess common equilibrium models and thermobarometric approaches. Under the studied conditions, our data suggest that the commonly applied Fe–Mg exchange ($^{cpx\text{-}melt}Kd_{Fe-Mg}$) is insensitive to increasing ΔT and may not be a reliable indicator of equilibrium. The combined use of DiHd ($CaMgSi_2O_6 + CaFeSi_2O_6$) and EnFs ($Mg_2Si_2O_6 + Fe_2Si_2O_6$) models indicate the attainment of equilibrium in both Al-rich and Al-poor zones for almost all investigated ΔT. In contrast, CaTs ($CaAl_2SiO_6$) and CaTi ($CaTiAl_2O_6$) models reveal substantial deviations from equilibrium with increasing ΔT, particularly in Al-rich zones. We postulate that this reflects slower diffusion of Al and Ti in the melt compared with Ca and Mg and recommend the concurrent application of these four models to evaluate equilibrium between clinopyroxene and melt, particularly for sector-zoned crystals.
Thermobarometers calibrated with only isothermal–isobaric experiments closely reproduce experimental *P*–*T* at low ΔT, equivalent to natural phenocrysts cores and sector-zoned mantles. Models that also consider decompression experiments are most accurate at high ΔT and are therefore suitable for outermost phenocryst rims and groundmass microlites. Recent machine learning approaches reproduce *P*–*T* conditions across all ΔT conditions. Applying our experimental constraints to sector-zoned microphenocrysts and groundmass microlites erupted during the 1974 eccentric eruption at Mt. Etna, we highlight that both hourglass and prism sectors are suitable for thermobarometry, given that equilibrium is sufficiently tested for. The combination of DiHd, EnFs, CaTs and CaTi models identifies compositions closest to equilibrium with the bulk melt composition, and results in smaller differences in *P*–*T* calculated for hourglass and prism sectors compared with applying only DiHd and EnFs equilibrium models. This provides a framework to assess crystallisation conditions recorded by sector-zoned clinopyroxene crystals in mafic alkaline settings.

Key words: undercooling; clinopyroxene; geothermobarometry; equilibrium models; sector zoning

INTRODUCTION

Thermobarometry provides a means to extract crystallisation pressures and temperatures from volcanic crystals. Understanding the storage conditions of magma is critical in unravelling the anatomy of a volcanic plumbing system (Cashman *et al.*, 2017; Putirka, 2017), which can be used in conjunction with geophysical data to improve hazard monitoring efforts (e.g. Longpré *et al.*, 2014). Clinopyroxene is a common mineral in a range of volcanic settings and has a composition that is highly sensitive to changes in pressure and temperature (Putirka, 2008; Mollo *et al.*, 2018). Coupled with slow lattice diffusion compared with other minerals, such as olivine (Müller *et al.*, 2013; Costa, 2021), and stability over a broad range of pressure, temperature and oxygen fugacity conditions (Armienti *et al.*, 2007), clinopyroxene is efficient at capturing changes in *P*–*T* conditions across a plumbing system. Clinopyroxene-based thermometers depend on chemical variables, with most popular models based on the temperature-sensitive exchange of the jadeite ($Jd = NaAlSi_2O_6$) and diopside–hedenbergite ($DiHd = CaMgSi_2O_6 + CaFeSi_2O_6$) components between clinopyroxene and melt (Putirka *et al.*, 1996; Putirka, 2008). The jadeite component of clinopyroxene is also highly sensitive to pressure, and many barometers utilise its solubility in clinopyroxene to determine crystallisation depth (Putirka *et al.*, 1996; Putirka, 2008). The calibration datasets of most thermobarometers are based on isothermal–isobaric experiments, although others also incorporate decompression experiments with clinopyroxene crystallising under variable undercooling conditions (Mollo *et al.*, 2018). In addition, recent machine

Received: April 25, 2023. **Revised:** August 24, 2023. **Accepted:** October 1, 2023

learning algorithms have provided alternative approaches to estimate crystallisation pressure and temperature using clinopyroxene compositions (Petrelli *et al.*, 2020; Jorgenson *et al.*, 2022). In most cases, it is critical to use an appropriate melt composition to approximate that from which clinopyroxene crystallised. There are several methods that assess the attainment of equilibrium between clinopyroxene and melt, including the exchange of Fe–Mg between clinopyroxene and melt ($^{cpx-melt}Kd_{Fe-Mg} = 0.28 \pm 0.08$; Putirka, 2008) and the comparison of measured clinopyroxene components with those predicted for clinopyroxene crystallising from the chosen melt composition under equilibrium crystallisation conditions (Putirka, 1999; Mollo *et al.*, 2013b).

Clinopyroxene growing from a single melt composition can exhibit different chemistries along distinct crystallographic axes (sector zoning), complicating the assessment of equilibrium and the application of thermobarometers. In sector-zoned clinopyroxene, c-axis parallel 'hourglass' sectors {−1 1 1} and c-axis perpendicular 'prism' sectors {*h k* 0} grow simultaneously with distinct chemical compositions, as illustrated in natural clinopyroxene by time-equivalent concentric zoning cross-cutting sector zoning (Leung, 1974; Dowty, 1976; Ubide *et al.*, 2019). Typically, prism sectors are enriched in Al + Ti and depleted in Si + Mg relative to hourglass sectors (Leung, 1974; Ubide *et al.*, 2019), following charge balance mechanisms qualitatively described for alkaline systems as:

$$\left[{}^{T}Si^{4+} + {}^{M1}Mg^{2+} + {}^{M1}Fe^{2+}\right]_{\{-1\ 1\ 1\}} \leftrightarrow \left[{}^{T}Al^{3+} + {}^{M1}Ti^{4+} + {}^{M1}Fe^{3+}\right]_{\{h\ k\ 0\}} \quad (1)$$

The development of sector zoning has been related to the degree of magma undercooling ($\Delta T = T_{liquidus} - T_{crystallisation}$), which acts as a thermodynamic driver of crystallisation (Kirkpatrick, 1981). Undercooling can be imposed by either magma cooling or by increasing the *liquidus* temperature (for example, via magma mixing or decompression-induced H_2O exsolution, Ubide *et al.*, 2021 and references therin). Typically, crystals with polyhedral morphologies and sector zoning grow under slow interface kinetics at $\Delta T < 40$ °C, and increasing ΔT results in the development of smaller crystals with hollow, skeletal and dendritic morphologies due to fast interface kinetics and increasing nucleation rates (Kouchi *et al.*, 1983; Shea & Hammer, 2013; Pontesilli *et al.*, 2019; Masotta *et al.*, 2020; MacDonald *et al.*, 2022; Colle *et al.*, 2023). Clinopyroxene grown at high ΔT may be out of equilibrium with the corresponding melt composition due to the development of concentration gradients in the melt and kinetic incorporation of non-essential structural constituents and may return inaccurate thermobarometry results (Mollo *et al.*, 2010). It is therefore crucial to evaluate the suitability of thermobarometric calibrations at different degrees of ΔT.

The compositional contrast between sectors in clinopyroxene further complicates the application of thermobarometry, because clinopyroxene components used in a range of models, such as DiHd, are also preferentially partitioned between sectors. Despite this challenge, thermobarometry has been applied to sector-zoned clinopyroxene from a number of volcanic settings, with authors using only hourglass sectors (Zhou *et al.*, 2021), prism sectors (Park *et al.*, 2022) or both sectors together (Neave *et al.*, 2019, Ubide *et al.*, 2019, 2023), following various equilibrium models. However, a systematic, experimental appraisal of the sector that best estimates conditions of crystallisation has been lacking to date. Phenocryst rims and groundmass microlites have also been a target of thermobarometry for tracking final magmatic pathways (e.g. Klügel *et al.*, 2015). Their formation during magma decompression and ascent may result in high degrees of ΔT and fast crystal growth, allowing for an increased uptake of Al, Ti and Na (Mollo *et al.*, 2010; Ubide & Kamber, 2018) that may potentially obscure *P*–*T* conditions and lead to large uncertainties when using thermobarometers based on isobaric–isothermal experiments (Mollo *et al.*, 2013a; Ubide *et al.*, 2019).

Here, we investigate the effectiveness of five equilibrium models and three thermobarometers on clinopyroxene crystals experimentally produced from a primitive alkaline basalt at Mt. Etna (Italy) under varying degrees of ΔT. Experimental crystals range in texture from euhedral with sector zoning (Al-rich prism and Al-poor hourglass sectors) to skeletal and dendritic with Al-rich skeletons and Al-poor overgrowths with increasing ΔT (Masotta *et al.*, 2020; MacDonald *et al.*, 2022). For the sake of simplicity, we hereafter refer to Al-rich skeletons and prism sectors as 'Al-rich zones' and Al-poor hourglass sectors and crystal overgrowths as 'Al-poor zones.' These experiments have not been previously used to calibrate thermobarometric models, providing an opportunity to independently assess the effect of ΔT and sector zoning on a range of thermobarometers published in the literature. Applying comprehensive spreadsheets (Mollo *et al.*, 2018) and python packages (Thermobar version 1.0.26, Wieser *et al.*, 2022), we assess the effectiveness of equilibrium models and thermobarometers with increasing ΔT, as well as between Al-rich and Al-poor zones. We then apply our approach to natural clinopyroxene from the 1974 eruption at Mt. Etna (Italy), including microphenocrysts, with resorbed cores, sector-zoned Cr-rich mantles and Cr-poor rims (often referred to as 'outermost rims'), as well as groundmass microlites. Finally, we provide recommendations for the application of clinopyroxene thermobarometry to varied crystal populations, including those characterised by sector zoning.

EXPERIMENTAL SETUP

We used a series of non-end loaded piston cylinder experiments (Table 1) conducted at the HP-HT Laboratory of Experimental Volcanology and Geophysics (HP–HT Lab) of the Istituto Nazionale di Geofisica e Vulcanologia (INGV) in Rome, Italy, described and characterised for major elements in Masotta *et al.* (2020), and further explored for trace elements and mineral–melt partitioning in MacDonald *et al.* (2022).

The starting composition was a synthesised glass from Mt. Maletto trachybasalt, one of the most primitive magmas erupted at Mt. Etna (Tanguy *et al.*, 1997). Deionised H_2O was added to hydrous experiments using a micro-syringe (2–4 wt %). Pt capsules were loaded into a 19 mm NaCl–pyrex–graphite–MgO assembly with an intrinsic oxygen fugacity of 2 log units above the Ni–NiO buffer (Masotta *et al.*, 2012), consistent with magmatic conditions at Mt. Etna (e.g. Giacomoni *et al.*, 2014). Experimental pressure conditions were achieved by cold pressurisation to a nominal value 10% higher than the target, after which the pressure was slowly decreased to the desired value (400 or 800 MPa). Experimental temperature was monitored using a C-type (W-5Re/W-26Re) thermocouple (± 3 °C). Experiments were first heated to the *superliquidus* temperature ($T_{superliquidus}$) of 1300 °C, at a constant rate of 80 °C/min. After 30 minutes, temperature was decreased at a cooling rate of 80 °C/min to a resting temperature (T_{rest} = 1200–1050 °C), which was kept constant for 24 hours. Experiments were subsequently quenched at a cooling rate of 100 °C/min. Undercooling conditions (ΔT = 25–233 °C) in the experiments were modulated by varying either T_{rest} or, the *liquidus* temperature (by varying melt-H_2O). The *liquidus* temperature was calculated for

Table 1: Experiments used in this study and their corresponding resting temperature, pressure, melt–H_2O content and undercooling (ΔT)

Experiment	Temperature (°C)	Pressure (MPa)	H_2O_{added} (wt %)	ΔT (°C)
UC4-1150b	1150	400	2	32
UC4-1100a	1100	400	0	123
UC4-1100b	1100	400	2	82
UC4-1100c	1100	400	4	25
UC4-1050a	1050	400	0	173
UC4-1050b	1050	400	2	132
UC4-1050c	1050	400	4	75
UC8-1200a	1200	800	0	83
UC8-1150a	1150	800	0	133
UC8-1100a	1100	800	0	183
UC8-1100b	1100	800	2	141
UC8-1050a	1050	800	0	233
UC8-1050b	1050	800	2	191

each experiment as a function of pressure, melt composition and melt-H_2O content using rhyolite-MELTS (v.1.2.0; Gualda *et al.*, 2012), as reported in Masotta *et al.* (2020).

ANALYTICAL METHODS

Major element compositions of experimental clinopyroxenes were determined by electron probe microanalysis (EPMA) at The University of Queensland Centre for Microscopy and Microanalysis (UQ-CMM), and at the HP-HT Lab in Rome.

At the UQ-CMM, we used a JEOL JXA-8200 microprobe equipped with five wavelength dispersive spectrometers. Data were collected using an accelerating voltage of 15 kV, a beam current of 15 nA and a fully focused beam, with an estimated interaction area of 2 × 2 μm. Counting times for elements were 10 seconds on peak and 5 seconds off peak. Matrix correction was undertaken using a ZAF (Z: atomic number; A: absorption; F: fluorescence) procedure. Calibration was performed using a range of standards: albite (Na–TAP and Al–TAP), wollastonite (Si–TAP and Ca–PETJ), chromite (Cr-PETJ and Fe–LIF), F-apatite (P-PETJ), Ni–olivine (Ni–LIF), olivine (Mg–TAP), orthoclase (K-PETJ), rutile (Ti–PETJ) and spessartine garnet (Mn–LIF). In addition to these, Kakanui augite, Lake Co feldspar and Springwater olivine (Jarosewich *et al.*, 1980) were routinely analysed throughout the analytical session to monitor data quality. Accuracy and precision, determined using secondary standards, were typically better than 3% and 2%, respectively, for elements with abundance >10 wt %; 7% and 5% for elements with abundance 1 to 10 wt %, and 15% and 8% for elements with abundance <1 wt % (Supplementary Table 1). We also assessed analytical precision using the EPMA-outputted uncertainty based on counting statistics for each analysis (Supplementary Table 2), as suggested in Wieser *et al.* (2023a). For analyses conducted at UQ-CMM, precision was typically better than 2% for elements with abundance >10 wt %; 5% for elements with abundance between 1 and 10 wt % and typically better than 15% for Na_2O.

Analyses performed at the HP-HT Lab used a JEOL JXA-8200, with an accelerating voltage of 15 kV, a beam current of 7.5 nA, and a fully focused beam (1–2 μm diameter). Elements were counted for 10s on peak and 5 s off peak. Calibration was performed using a range of standards from Micro-Analysis Consultants (MAC; http://www.macstandards.co.uk), including: albite (Si-PET, Al-TAP, Na-TAP), forsterite (Mg-TAP), augite (Fe-LIF), apatite (Ca-PET, P-PET), orthoclase (K-PET), rutile (Ti-PET), rhodonite (Mn-LIF) as well as JEOL Cr metal (Cr-PET). MAC augite and albite were used as a quality monitors. Accuracy and precision from secondary standards (Supplementary Table 1) were typically better than 1–5% for elements with abundance >1 wt %. For elements with abundance <1 wt %, accuracy was typically better than 1% to 10% (Supplementary Table 1). Analytical precision determined using EPMA outputted uncertainties on each analysis were typically better than 2% for elements with abundance >10 wt %, 5% for elements with abundance between 1 and 10 wt % and typically better than 7% for Na_2O (Supplementary Table 2).

Glass compositions were obtained at the HP-HT Lab using a slightly defocused beam (5 μm diameter) and are reported in Masotta *et al.* (2020).

EXPERIMENTAL CLINOPYROXENE CRYSTALS

Textural variations

Our set of experimentally produced clinopyroxene crystals exhibit significant variations in morphology with increasing ΔT.

At 400 MPa, experiments conducted at relatively low ΔT (ΔT = 25–32 °C) exhibit polyhedral morphologies (Fig. 1). Further increases in ΔT produce crystals with skeletal (ΔT = 75–123 °C) to dendritic morphologies (ΔT = 132–173 °C; Fig. 1). The shift in crystal morphology with ΔT is paired with a decrease in crystal size (from 560 μm length at ΔT = 25 °C to 130 μm length at ΔT = 173 °C) and growth rate at the expense of increasing crystallinity (5 to 29 vol % crystals; Masotta *et al.*, 2020).

At 800 MPa, the morphological evolution of experiments is similar. The lowest ΔT examined is ΔT = 82 °C, hence we did not produce polyhedral crystals. Similar to the 400 MPa experiments, increasing ΔT is associated with shifts in crystal morphology from skeletal (ΔT = 82–141 °C) to dendritic (ΔT = 183–233 °C), a decrease in crystal size (440 μm length at ΔT = 82 °C to 110 μm length at ΔT = 133 °C) and growth rate, and an increase in crystallinity (15–55 vol % crystals; Masotta *et al.*, 2020).

Major element compositions and zoning

Experimental clinopyroxene crystals exhibit distinct compositional zoning across all investigated ΔT conditions, as illustrated by back scattered electron images (Fig. 1). At low ΔT (ΔT = 25–32 °C), crystals are sector zoned, with prism sectors enriched in Al-Ti relative to hourglass sectors. As ΔT increases (ΔT > 32 °C), clinopyroxene crystals become progressively skeletal and dendritic, with Al-Ti rich skeletons and Al-Ti poor overgrowths, as described for

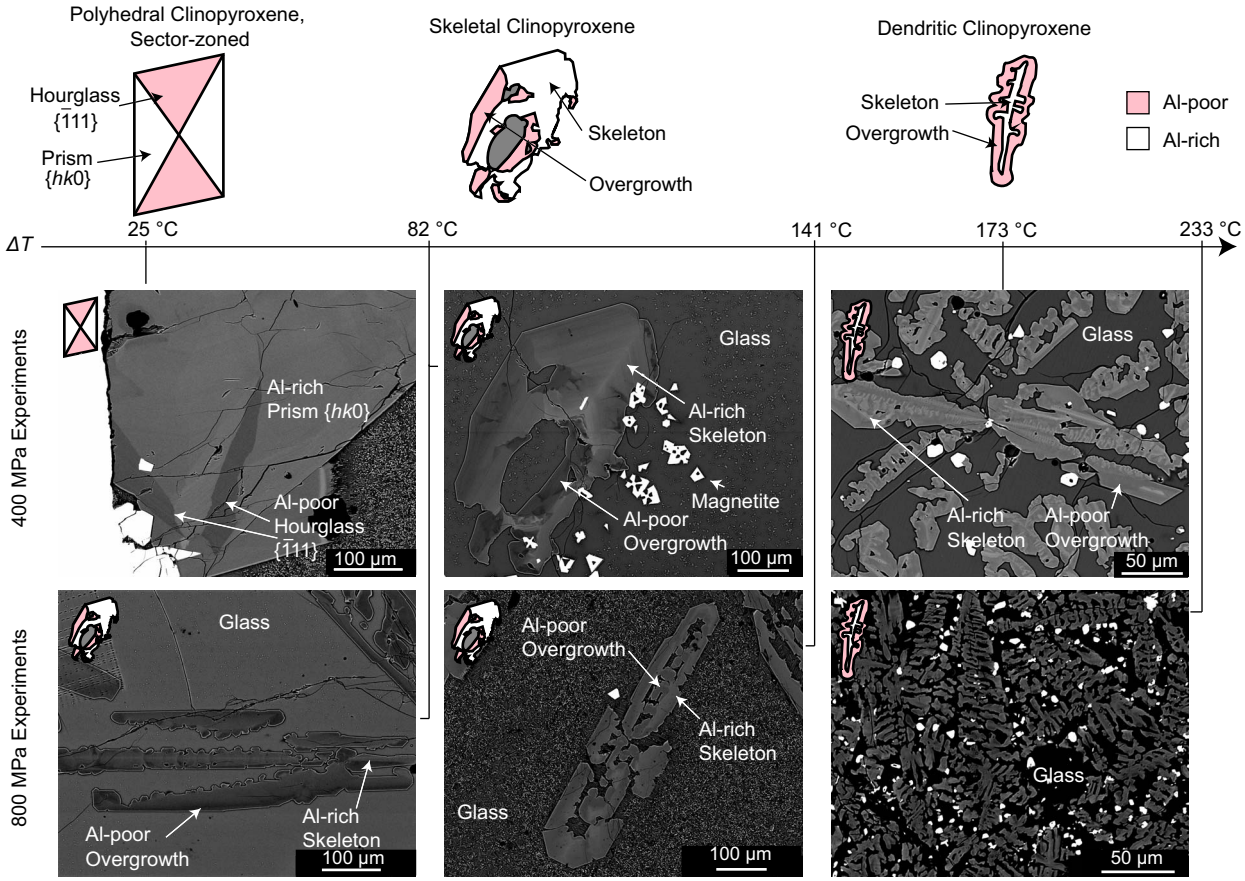

Fig. 1. Clinopyroxene morphology and zoning with increasing undercooling (ΔT). Back scattered electron images of clinopyroxene crystals produced in undercooling experiments at 400 MPa (first row) and 800 MPa (second row) show changes in morphology from polyhedral with sector zoning, to skeletal and dendritic with Al-rich skeletons and Al-poor overgrowths as ΔT increases.

a similar series of experiments in Pontesilli *et al.* (2019) and Colle *et al.* (2023).

Increasing ΔT influences clinopyroxene major element chemistry and clinopyroxene components, calculated using the procedure of Putirka (1999) (Fig. 2; data set provided in Supplementary Table 2). In accordance with the classification scheme of Morimoto (1988), our experimental clinopyroxene classifies as augite, or lies on the diopside–augite boundary (Fig. 2). In the experiments conducted at 400 MPa, as ΔT increases from 23 to 173 °C, Mg# [Mg# = 100 MgO / (MgO + FeO_t) on molar basis] and DiHd decrease (e.g. average $^{\text{Al-poor}}$Mg# = 82–71, $^{\text{Al-poor}}$DiHd = 0.83–0.65). In contrast, the enstatite-ferrosilite (EnFs = En + Fs; En, $Mg_2Si_2O_6$; Fs, $Fe_2Si_2O_6$), Ca-Tschermak (CaTs, $CaAl_2SiO_6$) and Jd components increase with ΔT (e.g. $^{\text{Al-poor}}$EnFs = 0.13–0.21, $^{\text{Al-poor}}$CaTs = 0.01–0.08, $^{\text{Al-poor}}$Jd = 0.02–0.05; see Supplementary Table 1 for additional data). Mg#, DiHd, EnFs and CaTs are also influenced by zoning in experimental crystals. Al-poor zones have higher average Mg# and DiHd, and lower EnFs and CaTs than their Al-rich counterparts (Fig. 2; e.g. at ΔT = 25 °C, $^{\text{Al-poor}}$DiHd = 0.68 and $^{\text{Al-rich}}$DiHd = 0.59). In contrast, Jd does not appear to preferentially partition as strongly between zones, with a difference typically <0.01 apfu (Supplementary Table 2). The relative enrichment of DiHd and depletion of CaTs and EnFs in Al-poor zones relative to Al-rich zones, and lack of zoning of Jd and hence, Na, is consistent with charge balancing substitution mechanisms described for sector zoning, as per Equation 1 (Ubide *et al.*, 2019).

Similar to the 400 MPa series of experiments, clinopyroxene crystallised in the 800 MPa suite of experiments have typically lower average DiHd and Mg# and higher EnFs with increasing ΔT (e.g. $^{\text{Al-poor}}$DiHd = 0.69–0.61, $^{\text{Al-poor}}$Mg# = 79–73, $^{\text{Al-poor}}$EnFs = 0.14–0.21 for ΔT = 83–233 °C; Fig. 2). Zoning also affects the composition of clinopyroxene as observed for the 400 MPa experiments (see Supplementary Table 2). However, unlike experiments conducted at 400 MPa, increasing ΔT does not affect CaTs or Jd (e.g. $^{\text{Al-poor}}$CaTs = 0.08 for ΔT = 83 and 233 °C, with a maximum of 0.1 at ΔT = 183 °C). This can be attributed to the greater uptake of Na and Al into the structure of clinopyroxene with increasing pressure (Blundy *et al.*, 1995; Müntener *et al.*, 2001), overwhelming the effect of kinetics induced by ΔT on clinopyroxene composition.

ASSESSMENT OF CLINOPYROXENE-MELT EQUILIBRIUM

Prior to the application of thermobarometers to clinopyroxene–melt pairs, their state of equilibrium needs to be assessed. A range of equilibrium models can be utilised for this purpose, and here we test five equations on our suite of ΔT experiments and individual Al-rich and Al-poor zones (Fig. 3). For the melt composition, we use glass compositions reported in Masotta *et al.* (2020) for the same set of experiments, which we also provide in Supplementary Table 3.

The Fe–Mg equilibrium model utilises the exchange of Fe and Mg between clinopyroxene and melt, with an equilibrium range of $^{\text{cpx–melt}}Kd_{\text{Fe–Mg}} = 0.28 \pm 0.08$ (Putirka, 2008) which we calculated using FeO_t for both clinopyroxene and melt. Applying this model, only some experimental clinopyroxene data plot within the

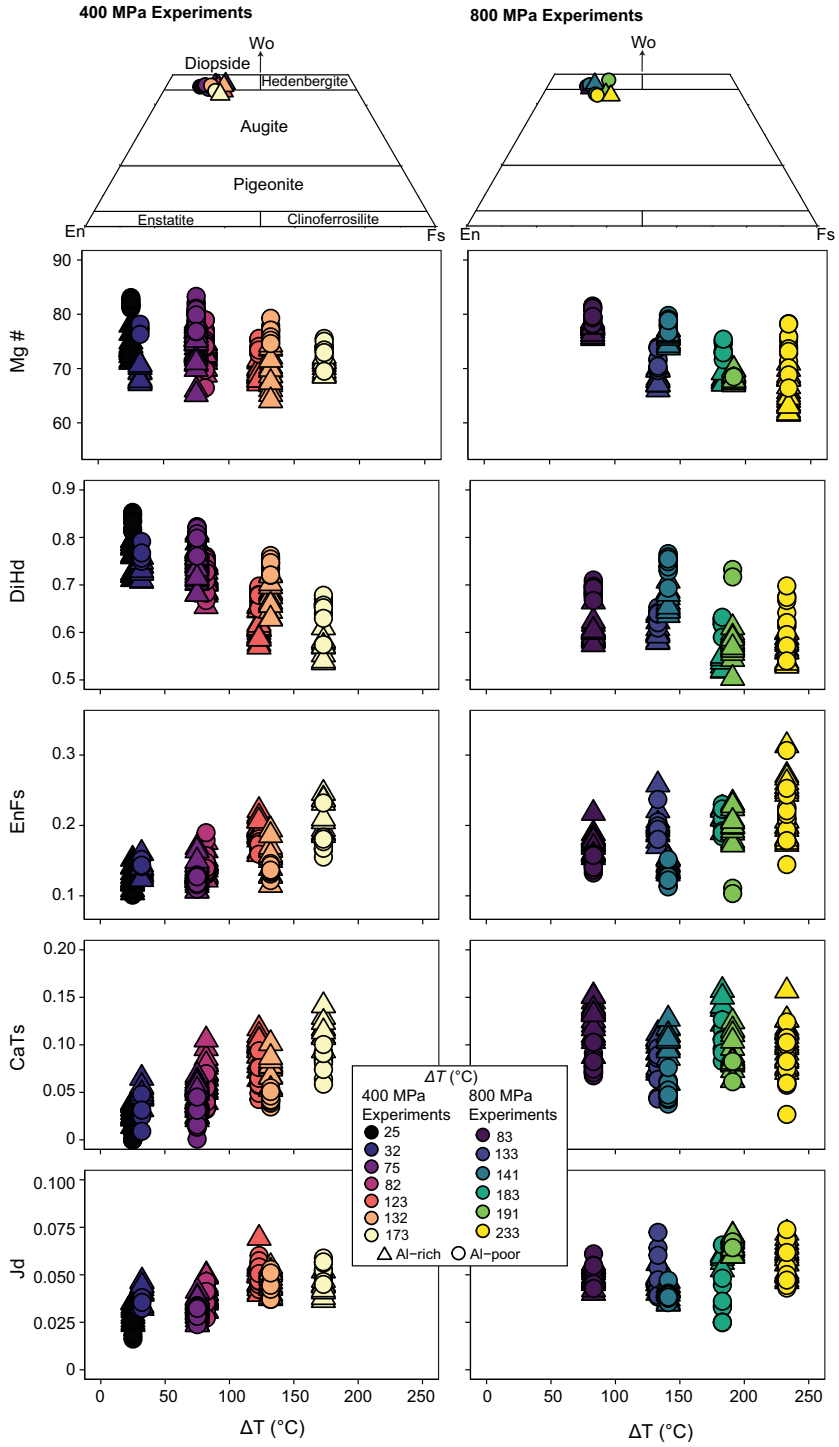

Fig. 2. Major element compositions of experimental clinopyroxene as a function of undercooling (ΔT). Ternary diagrams use the clinopyroxene classification scheme of Morimoto (1988). Data are split between 400 MPa experiments (left panels) and 800 MPa experiments (right panels).

equilibrium range (Fig. 3; Supplementary Table 4). Overall, as ΔT increases, crystallinity increases causing the Mg# of the melt to decrease, resulting in a lower predicted Mg# for clinopyroxene. Increasing ΔT from 25 to 173 °C at 400 MPa does not result in any systematic deviations from equilibrium. For example, clinopyroxene crystallised at $\Delta T = 173$ °C is almost entirely within the range of equilibrium ($^{\text{Al-rich}}\Delta^{\text{cpx–melt}}\text{Kd}_{\text{Fe–Mg}} = 0.09$; $^{\text{Al-poor}}\Delta^{\text{cpx–melt}}\text{Kd}_{\text{Fe–Mg}} = 0.04$), whereas $\Delta T = 32$ °C is almost entirely out of equilibrium ($^{\text{Al-rich}}\Delta^{\text{cpx–melt}}\text{Kd}_{\text{Fe–Mg}} = 0.33$; $^{\text{Al-poor}}\Delta^{\text{cpx–melt}}\text{Kd}_{\text{Fe–Mg}} = 0.12$; Fig. 1), and only Al-poor zones of clinopyroxene at $\Delta T = 25$ °C fall within the accepted equilibrium range (Fig. 3). This contradicts the expectation that increasing ΔT may produce clinopyroxene compositions out of equilibrium with the melt and suggests that the Fe–Mg exchange does not respond to varying ΔT. Comparable results are also observed at 800 MPa, where apparent disequilibrium and equilibrium conditions seem to be unrelated to ΔT. It has previously been proposed that $^{\text{cpx–melt}}\text{Kd}_{\text{Fe–Mg}}$ is insensitive to kinetic effects, returning equilibrium values for experiments produced at high cooling rates (Putirka, 2008; Mollo *et al.*, 2010; Mollo *et al.*, 2012).

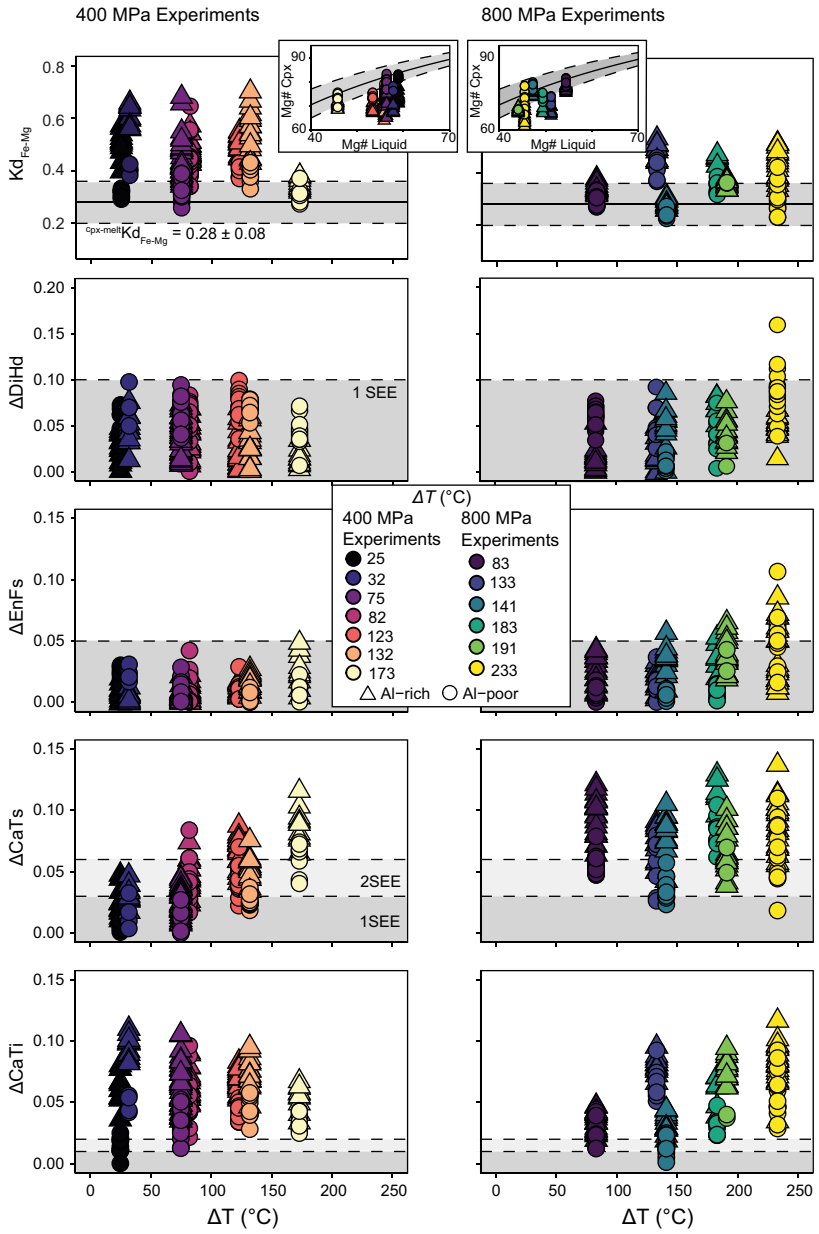

Fig. 3. Clinopyroxene – melt equilibrium modelling for experimental clinopyroxene and glass compositions, with input temperature calculated using Eq. 33 (Putirka, 2008). From top to bottom: $^{cpx-melt}Kd_{Fe-Mg}$; ΔDiHd, ΔEnFs, ΔCaTs and ΔCaTi (calculated as absolute values). Rhodes diagrams are also included as inserts. Grey fields indicate accepted equilibrium ranges and are expanded to 2SEE for CaTs and CaTi considering the lower correlation between calibration data sets relative to 1SEE of DiHd and EnFs (Putirka, 1999).

Indeed, the experimental assessment of $^{cpx-melt}Kd_{Fe-Mg}$ of Di Fiore *et al.* (2021) highlighted that the replacement of Si by Al in the tetrahedral site of clinopyroxene is accompanied by a variation in $^{cpx-melt}Kd_{Fe-Mg}$ under both interface- and diffusion-controlled growth, concluding that prescribing equilibrium to a narrow range of Fe–Mg values may not be representative of near-equilibrium growth conditions. Our calculations extend this finding to ΔT and its effects on the textural and compositional variation of clinopyroxene. Considering separately Al-rich and Al-poor zones, Al-rich zones typically lie further outside the equilibrium range of $^{cpx-melt}Kd_{Fe-Mg}$ compared to Al-poor zones in the same crystals (e.g. $^{Al\text{-}rich}\ \Delta^{cpx-melt}Kd_{Fe-Mg} = 0.24$; $^{Al\text{-}poor}\ \Delta^{cpx-melt}Kd_{Fe-Mg} = 0.05$ at $\Delta T = 25$ °C; Fig. 3). This can be accounted for by the higher incorporation of Al, Fe^{3+} and highly charged Ti cations into Al-rich zones, depressing the uptake of Mg as controlled by charge-balancing substitution mechanisms (Equation 1; see also Ubide *et al.*, 2019). Although this may suggest that Al-poor zones, such as hourglass sectors, better reflect equilibrium, the general insensitivity of $^{cpx-melt}Kd_{Fe-Mg}$ to kinetic effects and ΔT requires that other equilibrium models must be examined before making this conclusion.

The equilibrium model for DiHd developed by Putirka (1999) and later reappraised by Mollo *et al.* (2013b) is based on the difference (Δ) between DiHd measured in clinopyroxene and DiHd predicted for a given melt composition at specific *P*–*T* conditions. Here, we use an expanded equilibrium range of ±0.1 ΔDiHd, representative of near-equilibrium crystal growth conditions (Mollo *et al.*, 2018). The equilibrium models for EnFs (±0.05 ΔEnFs equilibrium range), CaTs (± 0.03 ΔCaTs equilibrium range) and CaTi (± 0.01 ΔCaTi equilibrium range) follow similar principles

(Putirka, 1999; Mollo *et al.*, 2013b). We note that the fit for the CaTs and CaTi equilibrium models, is poorer than those obtained for DiHd and EnFs (Putirka, 1999). In addition, our data set consists of zoned crystals, where the interface melt immediately feeding growing clinopyroxene faces may differ in composition from the far field melt (Masotta *et al.*, 2020), particularly for species that diffuse slowly in the melt. Therefore, we consider a broader range of equilibrium for the CaTs and CaTi models, equivalent to 2 SEE (i.e., standard error of estimate) of predicted values (± 0.06 ΔCaTs and ± 0.02 ΔCaTi).

At 400 MPa, DiHd and EnFs equilibrium models attest to the attainment of local interface equilibrium between clinopyroxene and melt for all ΔT conditions investigated (Fig. 3, Supplementary Figure 1), with no significant differences between Al-rich and Al-poor zones (e.g. $^{\text{Al-rich}}\Delta\text{DiHd} = 0.03$ and $^{\text{Al-poor}}\Delta\text{DiHd} = 0.04$ at $\Delta T = 25$ °C). At 800 MPa, results are similar, except at high ΔT (183–233 °C), where Al-poor zones deviate from DiHd equilibrium and both Al-rich and Al-poor zones deviate from EnFs equilibrium. Overall, this suggests the attainment of local interface equilibrium, for DiHd and EnFs in both Al–rich and Al–poor crystal zones up to $\Delta T = 200$ °C, corresponding to high degrees of crystallinity and dendritic morphologies.

In contrast, the CaTs model shows that our clinopyroxene–melt pairs are not in equilibrium at high ΔT (82–173 °C) at 400 MPa and are typically not in equilibrium for all investigated ΔT at 800 MPa. In addition, Al-rich zones have higher ΔCaTs than Al-poor zones (e.g. $^{\text{Al-rich}}\Delta\text{CaTs} = 0.02$ and $^{\text{Al-poor}}\Delta\text{CaTs} = 0.008$ at $\Delta T = 25$ °C; Fig. 3). Therefore, unlike the DiHd and EnFs models, the CaTs model appears to be more sensitive to both ΔT and zoning of Al. The CaTi model shows a more exaggerated effect for both ΔT and zone type; at 400 MPa, the majority of our clinopyroxene–melt pairs have ΔCaTi that exceed the equilibrium range (Fig. 3). The only set that consistently attain equilibrium in accordance with CaTi are the Al-poor zones from the lowest ΔT experiment ($^{\text{Al-rich}}\Delta\text{CaTi} = 0.06$ and $^{\text{Al-poor}}\Delta\text{CaTi} = 0.01$ at $\Delta T = 25$ °C), whereas at higher ΔT, all clinopyroxene–melt pairs are in CaTi disequilibrium (e.g. $^{\text{Al-rich}}\Delta\text{CaTi} = 0.05$ and $^{\text{Al-poor}}\Delta\text{CaTi} = 0.03$ at $\Delta T = 173$ °C). Similarly, at 800 MPa, most experimental clinopyroxene–melt pairs are out of CaTi equilibrium. To explore why the CaTs and CaTi models appear to give results which conflict with the DiHd and EnFs models, we consider growth under low ΔT (25–32 °C) and high ΔT (> 32 °C) separately.

For the case of polyhedral, sector-zoned clinopyroxene, which we observe at low ΔT and only at 400 MPa, Al-rich prism sectors have CaTs compositions that fall either within the accepted range of the equilibrium model ($^{\text{Al-rich}}\Delta\text{CaTs} = 0.02$ at $\Delta T = 25$ °C) or just outside of the 1 SEE equilibrium range ($^{\text{Al-rich}}\Delta\text{CaTs} = 0.03$ at $\Delta T = 32$ °C) as ΔT increases. On the other hand, Al-poor zones typically exhibit compositions closer to equilibrium and within 1 SEE of the equilibrium range ($^{\text{Al-poor}}\Delta\text{CaTs} = 0.008$ and 0.015 at $\Delta T = 25$ °C and 32 °C, respectively). For CaTi, only Al-poor zones at $\Delta T = 25$ °C, are on average, within 2 SEE of the equilibrium range (Fig. 3), whereas Al-rich zones are out of equilibrium at the same ΔT, as outlined previously. Increasing ΔT pushes ΔCaTi further from the equilibrium range, suggesting that both Al-rich and Al-poor zones did not achieve equilibrium with the melt ($^{\text{Al-rich}}\Delta\text{CaTi} = 0.09$; $^{\text{Al-poor}}\Delta\text{CaTi} = 0.05$ at $\Delta T = 32$ °C). Therefore, although both zone types indicate the attainment of local interface equilibrium in accordance with DiHd and EnFs equilibrium models, progressive departure from the accepted range of CaTs equilibrium values between zone types may reflect compositional differences in the local melt feeding growth along different crystal faces. This may also account for the behaviour of ΔCaTi between zones and with increasing ΔT. Sector zoning is attributed to a combination of the geometric arrangement and relative growth rates of crystal faces between sectors and the diffusion of cations in the melt (Nakamura, 1973; Downes, 1974; Leung, 1974; Dowty, 1976). Slow growing {*h k* 0} sectors, which have alternating exposed T, M1 and M2 sites, require large quantities of Si and Mg to facilitate growth. The rapid depletion of these species in the interface melt results in an enrichment of incompatible cations, such as Al and Ti, which are subsequently incorporated into the lattice sites. On the other hand, the fast growing {−1 1 1} sector has simultaneously exposed M– and T– sites, which limits the incorporation of incompatible cations (Hollister & Gancarz, 1971; Dowty, 1976). The interface melts feeding the growth of sectors become progressively depleted in the cations feeding crystal growth, producing gradients driving the diffusive transport of cations between crystal faces (Leung, 1974). Therefore, the concurrent growth of hourglass and prisms sectors may be fed by local melts which differ from the bulk, far field melt in terms of essential structural constituents for clinopyroxene. In our experiments, this effect appears to indicate that hourglass sectors crystallising at $\Delta T \leq 25$ °C may be fed by a melt that is well approximated by the bulk far field melt composition. This may be crucial when assessing equilibrium in natural samples, where melt compositions are approximated using bulk rock or groundmass compositions.

On the other hand, at $\Delta T > 75$ °C under diffusion–controlled regimes, the growth of clinopyroxene exceeds the rate of diffusion of cations to the advancing melt surface (Dowty, 1980; Kirkpatrick, 1981). In this case, clinopyroxene growth is largely rate limited by the slow diffusion of Al and Ti cations in the melt, which concentrate at the crystal–melt interface and do not have enough time to re-equilibrate with the far field melt (Iezzi *et al.*, 2008, Iezzi *et al.*, 2011, Mollo *et al.*, 2012). On the other hand, Ca and Mg diffuse more rapidly in the melt (Zhang *et al.*, 2010), and therefore can re–equilibrate with the far field melt. It follows that although local equilibrium may be established for Ca and Mg (e.g., DiHd and EnFs), clinopyroxene growing at very high ΔT may incorporate disequilibrium proportions of Al and Ti impurity cations (e.g., CaTs and CaTi) due to the enrichment of these slow–diffusing chemical species at the crystal–melt interface.

Therefore, we propose that testing for clinopyroxene–melt equilibrium using solely DiHd and EnFs models may not be sufficient to determine if equilibrium is attained for all clinopyroxene components. In the case of sector-zoned clinopyroxene with polyhedral morphologies, the attainment, or lack, of CaTs and CaTi equilibrium may be attributed to local differences in crystal–melt interface compositions, and all sectors should be tested for equilibrium with putative melt compositions, as we explore in our examination of natural crystals ('Implications for Natural Clinopyroxene').

ASSESSMENT OF THERMOBAROMETRIC APPROACHES

We apply three different thermobarometers to our experimental clinopyroxene and melt compositions to assess the sensitivity of thermobarometry to magma undercooling and compositional zoning These were selected to represent different approaches to calculating crystallisation *P–T* conditions from clinopyroxene and melt compositional data. We filter clinopyroxene–melt pairs on the basis on of DiHd and EnFs equilibrium models, and CaTs and CaTi equilibrium models separately (as denoted by white circles in

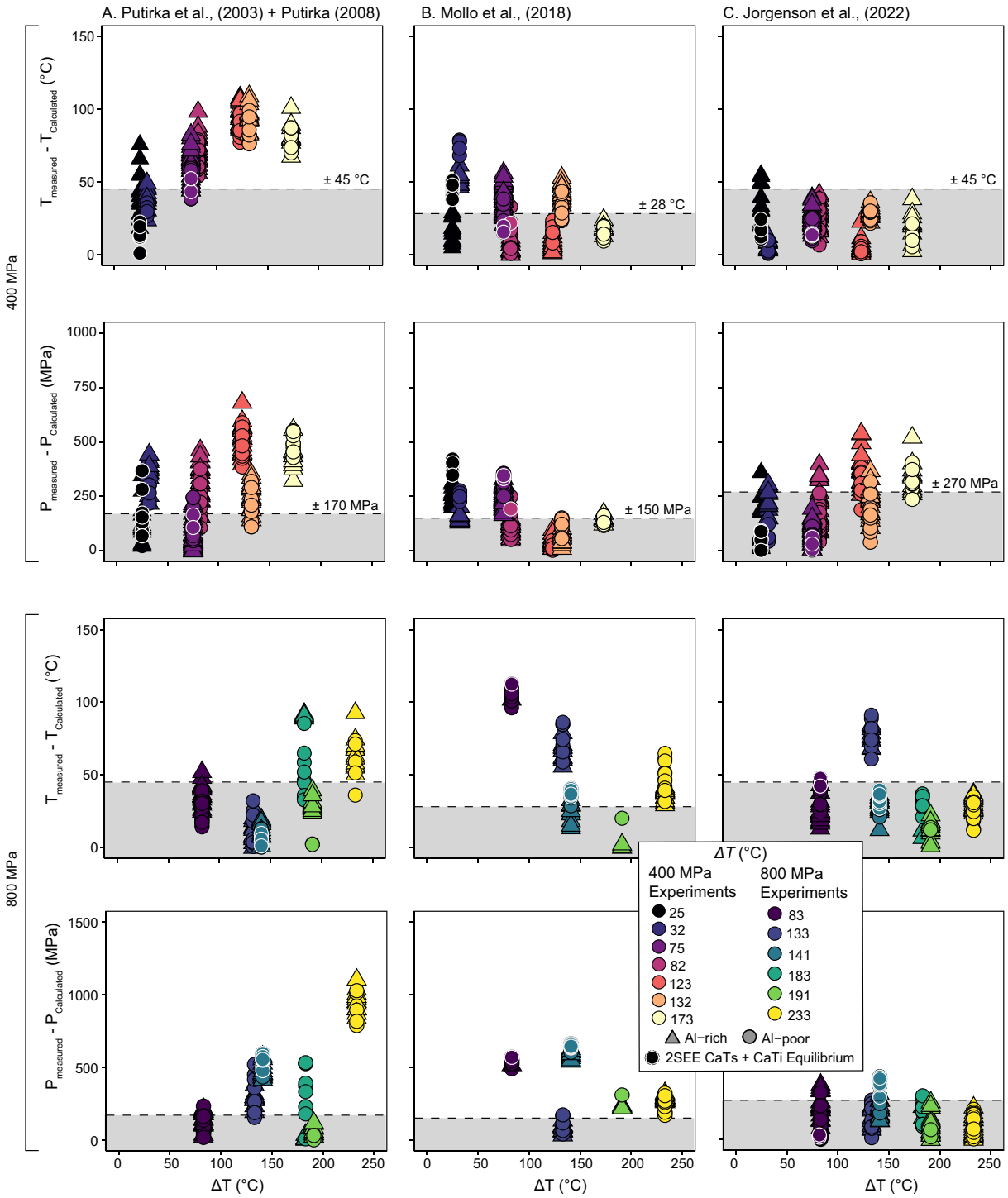

Fig. 4. Thermobarometry of experimental clinopyroxene–melt pairs using three different models; Thermobarometer A (Putirka *et al.*, 2003; Putirka, 2008), Thermobarometer B (Mollo *et al.*, 2018) and Thermobarometer C (Jorgenson *et al.*, 2022). Differences between measured and calculated pressure and temperature are compared to undercooling (ΔT) for both 400 and 800 MPa experiments to determine the effect of undercooling and sector zoning on the calculation of pressure and temperature. Data which also pass CaTi and CaTs equilibrium conditions are denoted by white outlines.

Fig. 4) to explore how additional filtering based on CaTs and CaTi modelling may influence calculated conditions of crystallisation. We also propagate errors from EPMA outputted uncertainties using Thermobar (Wieser *et al.*, 2022) for Models A and C. We note that propagated errors are consistently less than the reported model uncertainties and do not explain the trends we observe here (see Supplementary Table 4).

Model A: Isobaric–isothermal thermobarometry

We first consider the results obtained by iteratively solving Equation 33 of Putirka (2008) for temperature with Equation A of Putirka *et al.* (2003) for pressure, using the python package Thermobar (Wieser *et al.*, 2022). These equations were formulated by regression of selected clinopyroxene and melt components from a range of isobaric and isothermal experiments, spanning a range

of compositions and *P*–*T* conditions (Putirka *et al.*, 2003; Putirka, 2008). For simplicity, this combination will hereafter be referred to as 'Model A: Isobaric–Isothermal Thermobarometer.' A range of similar approaches are available in the literature, however this combination of isothermal–isobaric calibrations is considered a good predictor for mafic alkaline compositions (Mollo *et al.*, 2018), relevant to Mt. Etna compositions and hence, to our suite of experiments. Our experiments return *P*–*T* results in overall agreement with experimental values at low ΔT and deviate from experimental values at high ΔT, as the thermobarometer begins to overestimate *P* and *T* (Fig. 4, Supplementary Table 4). Therefore, this model should return best results for clinopyroxene grown at low ΔT, including phenocryst cores and sector-zoned crystal populations.

At 400 MPa, the difference between the measured experimental temperature and the calculated temperature ($T_{diff} = |T_{measured} - T_{calculated}|$) increases beyond the model uncertainty (±45 °C) as ΔT increases from 25 to 173 °C. Specifically, average T_{diff} increases from 15 to 79 °C, and from 44 to 82 °C in Al-poor and Al-rich zones, respectively, with increasing ΔT. The increase in T_{diff} with ΔT observed in our experiments can be attributed to the key parameters upon which Equation 33 of Putirka (2008) is based, that is, the exchange of DiHd–Jd between clinopyroxene and melt, which is temperature–sensitive (Putirka *et al.*, 1996). Increasing Jd in clinopyroxene is associated with a decrease in $T_{calculated}$, and conversely, increasing DiHd is associated with an increase in $T_{calculated}$ (Putirka, 2008). As described in 'Major Element Compositions and Zoning,' increasing ΔT results in an overall increase in Jd and decrease in DiHd (Fig. 1) and correlates with T_{diff} (Supplementary Figure 2), which initially suggest a decrease in $T_{calculated}$. However, we observe the opposite; as ΔT increases, $T_{calculated}$ also increases (Supplementary Table 4). To explain this result, we note that the composition of the melt also has a strong role in Equation 33. In particular, the mole fraction of SiO_2 and CaO in the melt ($X^{melt}_{SiO_2} X^{melt}_{CaO}$; Putirka, 2008), has a substantially larger influence on $T_{calculated}$ than the composition of clinopyroxene. Increasing ΔT results in an increase in $X^{melt}_{SiO_2}$ of 8% and a decrease in X^{melt}_{CaO} of 50%, causing an overall decrease in $X^{melt}_{SiO_2} X^{melt}_{CaO}$ (Supplementary Figure 3). The significant decrease in melt CaO with increasing ΔT is consistent with the increase in crystallinity. Higher degrees of clinopyroxene nucleation cause a depletion in major cations such as Ca in the melt, as they are rapidly consumed to produce new crystals. On the other hand, Si is slightly enriched in the melt due to an increase in ^{T}Al (following Equation 1) in clinopyroxene. Due to the decrease in molar fraction of CaO in the melt, $T_{calculated}$ increases with ΔT, becoming less accurate (Fig. 4; Supplementary Table 4).

Another key factor to note is the presence of H_2O in the melt, as $T_{calculated}$ is also dependent on melt-H_2O, which varies in our experiments from 0 to 4 wt %. Overall, the correlation between melt-H_2O and T_{diff} is weak ($R^2 = 0.4$; Supplementary Figure 2) and should only have a minor impact on our observations. However, as increasing melt–H_2O depresses the liquidus of clinopyroxene, which reduces ΔT, we also assess the role of H_2O-induced ΔT (Supplementary Figure 4). We only consider a set of experiments with the same T_{rest}, but varying melt-H_2O, to isolate the effect of melt-H_2O on ΔT. At $T_{rest} = 1100$ °C, increasing ΔT from 25 to 123 °C by decreasing melt-H_2O from 4 to 0 wt % results in an increase in T_{diff} in both Al-poor zones ($^{Al\text{-}poor}T_{diff}$ increases from 15 to 89 °C) and Al-rich zones ($^{Al\text{-}rich}T_{diff}$ increases from 44 to 98 °C).

We also investigate *T*-induced ΔT, which is achieved by isolating the effect of T_{rest} on ΔT by only considering experiments with the same melt-H_2O ($H_2O = 2$ wt. %). Similar to H_2O-induced ΔT, as ΔT increases with decreasing T_{rest}, T_{diff} increases (as ΔT increases from 32 to 132 °C, $^{Al\text{-}poor}T_{diff}$ increases from 31 to 84 °C, and $^{Al\text{-}rich}T_{diff}$ increases from 39 to 96 °C). Therefore, it can be surmised that both *T*-induced and H_2O-induced ΔT cause the same changes in T_{diff}.

A critical observation is that T_{diff}, on average, is within the range of model uncertainty for both Al-rich and Al-poor zones at $\Delta T \leq 32$ °C, corresponding to sector–zoned experimental crystals. Considering these experiments in detail, Al-poor hourglass have typically lower T_{diff} than Al-rich prism sectors ($^{Al\text{-}poor}T_{diff} = 15$ °C and $^{Al\text{-}rich}T_{diff} = 44$ °C) and show CaTs and CaTi components in equilibrium with the melt (Fig. 4), suggesting that hourglass sectors may be more suitable for thermometry. However, as T_{diff} is, on average, less than the model uncertainty (±45 °C) for both hourglass and prism sectors, we conclude that both sectors provide reliable estimates of crystallisation temperature. The application of more rigorous CaTs and CaTi equilibrium models may provide a means of further constraining temperature estimates, which we explore in 'Implications For Natural Clinopyroxene.'

We also explore the difference between measured and calculated pressure ($P_{diff} = P_{measured} - P_{calculated}$) for Model A. As ΔT increases from 25 to 173 °C, P_{diff} typically increases in Al-poor ($^{Al\text{-}poor}P_{diff}$ from 153 to 483 MPa) and Al-rich ($^{Al\text{-}rich}P_{diff}$ from 133 to 432 MPa) zones (Fig. 4). The key parameter controlling the value of $P_{calculated}$ for Model A is the Jd component of clinopyroxene. As illustrated in Fig. 2, increasing ΔT results in an overall increase in the Jd component of clinopyroxene, which results in the observed increase in P_{diff} with ΔT (Fig. 4). A principal observation from Fig. 4 is that the relationship between ΔT and P_{diff} is not as well-defined as it is for T_{diff}, as highlighted by the weaker correlation between ΔT and P_{diff} relative to ΔT-T_{diff} (Supplementary Figure 2). To further investigate the potential cause of this, as before, we investigate the role of H_2O-induced and *T*-induced ΔT. For the case of H_2O-induced ΔT, increasing ΔT by decreasing melt – H_2O results in an increase in P_{diff} (Supplementary Figure 4). However, when ΔT is increased by decreasing T_{rest} (*T*-induced ΔT), P_{diff} decreases, demonstrating that for the calculation of pressure, H_2O-induced and *T*-induced ΔT influence P_{diff} differently. Pressure, as calculated using Model A, is dependent on $T_{calculated}$. As ΔT decreases with $T_{measured}$, if $T_{calculated}$ is also decreasing, then it follows from Equation A of Putirka *et al.* (2003) that $P_{calculated}$ will also decrease, causing a decrease in P_{diff}. Indeed, this is what we observe when comparing the average $T_{calculated}$ and $P_{calculated}$ for *T*-induced ΔT (as ΔT increases from 32 to 132 °C, $T_{calculated}$ decreases from 1180 to 1099 °C and $P_{calculated}$ decreases from 672 to 598 MPa in Al-poor zones; Supplementary Table 4). Fitting regression lines to our data set also agrees with these results; values for the coefficient of determination (R^2) calculated for T-induced ΔT are much lower ($R^2 = 0.20$) than for H_2O-induced ΔT ($R^2 = 0.71$; Supplementary Figure 4), indicating that H_2O-induced ΔT is more influential on the resulting P_{diff}. Therefore, the behaviour of P_{diff} with ΔT is a consequence of the conflicting roles of changing *T*-induced and H_2O-induced ΔT. This implies that at our investigated conditions, crystals grown under ΔT induced solely by magma cooling (e.g. conditions of magma storage) may still provide reliable estimates of pressure using isothermal–isobaric thermobarometry. On the other hand, clinopyroxene crystallised under ΔT induced by H_2O exsolution from the melt (e.g. degassing during magma ascent) may not provide realistic estimates of crystallisation pressures calculated using Model A.

For comparison, we also consider *P*–*T* results obtained by iteratively solving Equation 33 of Putirka (2008) for *T* with Equation 31 of Putirka (2008) for *P* (Supplementary Figure 5). The relationship between T_{diff} and ΔT follows a similar pattern to that of Model A,

however T_{diff} is on average larger (e.g. at $\Delta T = 132$ °C, $^{Al\text{-}poor}T_{diff} = 112$ °C and $^{Al\text{-}rich}T_{diff} = 127$ °C; Supplementary Table 4). In contrast, the relationship between P_{diff} and ΔT noticeably differs between the two models. Only hourglass and some prism compositions from the lowest ΔT experiment have P_{diff} within the uncertainty of the model (± 290 MPa SEE). Most significantly, P_{diff} calculated using Equation 31 of Putirka (2008) yields P_{diff} which increases regardless of T-induced or H_2O-induced ΔT, but is typically larger (e.g. at $\Delta T = 132$ °C, $^{Al\text{-}poor}P_{diff} = 804$ MPa and $^{Al\text{-}rich}P_{diff} = 804$ MPa; Supplementary Table 4). A critical difference between these equations is that the calculation of pressure using Equations 31 + 33 of Putirka (2008) uses melt-H_2O, whereas Model A does not. We postulate that the consideration of melt-H_2O may lower the competing influences of H_2O- and T- induced ΔT.

To assess the suitability of hourglass or prism sectors for barometry, we consider only the experiments with sector-zoned crystals associated with low ΔT. On average, P_{diff} is lower than the uncertainty of Model A (± 170 MPa SEE calculated from calibration data; ± 480 MPa SEE calculated from a test data set) for Al-poor zones ($^{Al\text{-}poor}P_{diff} = 152$ MPa) and Al-rich zones ($^{Al\text{-}rich}P_{diff} = 132$ MPa) at $\Delta T = 25$ °C, however we note that the variation in P_{diff} is large for both zone types (Fig. 4), demonstrating a large variability in $P_{calculated}$. At $\Delta T = 32$ °C, neither the Al-rich hourglass sectors nor the Al-poor prism sectors return P_{diff} within the accepted uncertainty range of 170 MPa ($^{Al\text{-}poor}P_{diff} = 272$ MPa and $^{Al\text{-}rich}P_{diff} = 359$ MPa). We note that at this undercooling, neither Al-rich or Al-poor zones have ΔCaTi <0.02, highlighting that sector-zoned crystals which do not satisfy this requirement may provide estimates of P which deviate more strongly from actual P. Regardless, our results highlight that using thermobarometers based on isothermal–isobaric experimental data sets are only appropriate at low ΔT, such as for sector-zoned clinopyroxene.

At 800 MPa, as ΔT increases from 83 to 233 °C, T_{diff} for Al-poor zones increases from 24 to 58 °C and from 38 to 65 °C. Although T_{diff} typically increases with ΔT, only results at $\Delta T = 183$ and 233 °C are on average greater than the model uncertainty (Fig. 4), contrasting with 400 MPa experiments where T_{diff} exceeds uncertainty at $\Delta T > 32$ °C. It is critical to note that most experiments comprising the calibration data set for the thermobarometer of Putirka *et al.* (2003) were conducted at pressures >1 GPa. It follows then, that our experiments at 800 MPa may better reproduce crystallisation temperature via clinopyroxene–melt thermobarometry, even at ΔT consistent with growth of skeletal clinopyroxene, than the set of experiments at 400 MPa. Therefore, we anticipate that Model A should accurately reproduce conditions of deep crystallisation.

Unlike for 400 MPa, it is difficult to compare the relative roles of T-induced and H_2O-induced ΔT, as experiments conducted at 800 MPa only had at most up to two experiments at the same T_{rest} (Table 1). On the other hand, similar to our experiments at 400 MPa, P_{diff} at 800 MPa typically increases with increasing ΔT (Fig. 4; Supplementary Table 4). The only exception to this is at $\Delta T = 191$ °C, which we postulate may be due to the addition of 2 wt % H_2O at low temperature ($T_{rest} = 1050$ °C) being more effective at limiting the kinetic growth of clinopyroxene by enhancing melt diffusion components. For Al-poor zones, P_{diff} increases from 100 to 956 MPa as ΔT increases from 83 to 233 °C, and P_{diff} in Al-rich zones increases from 149 to 959 MPa. The significant difference between $P_{measured}$ and $P_{calculated}$ produced at high ΔT suggests that at high pressure, ΔT has a significant impact on P_{diff}, even if T_{diff} is not as strongly affected (e.g. at $\Delta T = 233$, $T_{calculated}$ is 6% higher than $T_{measured}$, but $P_{calculated}$ is 114% higher than $P_{measured}$).

As for the 400 MPa experiments, we also iteratively calculate P–T for the 800 MPa experiments using Equation 33 of Putirka (2008) and Equation 31 of Putirka (2008; Supplementary Figure 5). The relationship between T_{diff} and ΔT at 800 MPa is similar to 400 MPa, except for $\Delta T = 233$ °C, which returns T_{diff} within the uncertainty of the model. As $T_{calculated}$ here is determined using the same equation as Model A, we consider results of P_{diff} to ascertain the cause of this behaviour. For most experiments, P_{diff} is greater than the uncertainty of the model. The exceptions to this are $\Delta T = 141$ and 233 °C, which have P_{diff} less than the model uncertainty. Most Al-poor, and some Al-rich compositions from the $\Delta T = 141$ °C experiment satisfy the additional CaTs and CaTi tests, suggestive of compositions closer to equilibrium and more accurate PT estimates. This leaves the experiment $\Delta T = 233$ °C as an outlier, similar to what we observed for T_{diff}. Unlike Equation A of Putirka *et al.* (2003), Equation 31 of Putirka (2008) is highly dependent on the square of the sum of the mole fraction of Na_2O and K_2O. We note that the melt composition obtained at $\Delta T = 233$ °C has significantly higher content of these constituents than other experiments at 800 MPa (see Supplementary Table 4). As Na_2O and K_2O are negatively correlated with P, this results in a lower $P_{calculated}$ relative to the other 800 MPa experiments, accounting for the lower P_{diff} and T_{diff}.

Model B: Decompression and undercooling thermobarometry

Model A was later refined by Mollo *et al.* (2018) for mafic alkaline compositions specifically, with a calibration data set that included clinopyroxene crystallised during decompression and magma ΔT, with uncertainties of ± 28 °C and ± 150 MPa (SEE calculated from the calibration data set; test data set yielded regression statistics of ± 15 °C and ± 116 MPa) for temperature and pressure, respectively. Hereafter, we refer to this calibration as 'Model B: Decompression and Undercooling Thermobarometer'. Consistent with the calibration data set, our experiments return more accurate P–T results at high ΔT using this model, whereas low ΔT experiments systematically underestimate P–T (Fig. 4, Supplementary Table 4). This contrasts with results from Model A, indicating that Model B should return best results for phenocryst rims and groundmass microlites in natural samples.

For the 400 MPa suite of experiments, overall T_{diff} decreases as ΔT increases from 23 to 173 °C, and typically underestimates T at low ΔT (see Supplementary Table 4). In Al-poor zones, T_{diff} decreases from 44 to 15 °C as ΔT increases, but $^{Al\text{-}rich}T_{diff}$ does not systematically change with increasing ΔT. Average T_{diff} is similar at both the highest and lowest ΔT conditions investigated (for $\Delta T = 23$ and 173 °C, $^{Al\text{-}rich}T_{diff} = 16$ and 19 °C respectively), and is highest at $\Delta T = 32$ °C ($^{Al\text{-}rich}T_{diff} = 52$ °C). This corresponds to a weak relationship between T_{diff} and ΔT for both T-induced and H_2O-induced ΔT (Supplementary Figure 4). Critically, the overall relationship between T_{diff} and ΔT observed when using Model B starkly contrasts with Model A; in the latter ΔT and T_{diff} increase concurrently. Although this may suggest one model is erroneous, this can be reconciled by considering the differences in the data sets used to calibrate these models. Model A uses an experimental data set which approximates conditions of isobaric-isothermal crystal growth. On the other hand, Model B also includes experiments which were conducted at variable decompression and ΔT conditions to reproduce conditions of ascent (Mollo *et al.*, 2018), and is therefore able to reproduce crystallisation temperature for high ΔT conditions.

For pressure, P_{diff} behaves in broadly the same way as T_{diff} with ΔT; high ΔT clinopyroxene–melt compositions provide more accurate estimates of crystallisation pressure than those from low

ΔT experiments, which underestimate P (Fig. 4). In Al-poor zones, P_{diff} decreases from 377 to 141 MPa with increasing ΔT, and in Al-rich zones, P_{diff} decreases from 255 to 150 MPa. As for Model A, ΔT induced by changing the H_2O content of the melt more strongly correlates with P_{diff} than T-induced ΔT. This highlights that, unlike Model A, crystals grown under H_2O-induced ΔT may give more reliable estimates of pressure using Model B. Overall, our results suggest that Model A may be most suitable for low ΔT clinopyroxene crystallising at isobaric-isothermal conditions, and Model B can predict more accurate crystallisation conditions at high ΔT. We explore the implications for this using natural crystals in 'Implications For Natural Clinopyroxene.'

At 800 MPa, T_{diff} typically decreases with ΔT, in both Al-rich and Al-poor zones ($^{\text{Al-poor}}T_{diff}$ decreases from 105 to 48 °C and $^{\text{Al-rich}}T_{diff}$ decreases from 102 to 37 °C as ΔT increases from 83 to 233 °C), similar to results at 400 MPa. However, in detail, T_{diff} is typically much larger at 800 MPa than 400 MPa (Fig. 4). The calibration data set of Mollo *et al.* (2018) incorporates predominately low-pressure experiments at $P \leq 400$ MPa. We postulate that the larger T_{diff} we observe reflects the bias of the data set towards low pressure crystallisation conditions. Similarly, although P_{diff} also decreases overall with ΔT ($^{\text{Al-poor}}P_{diff}$ decreases from 537 to 15 MPa and $^{\text{Al-rich}}P_{diff}$ decreases from 519 to 73 MPa as ΔT increases from 83 to 191 °C), most Model B estimates using high pressure ΔT experiments are not able to faithfully reproduce experimental pressure conditions (Fig. 4). We note P_{diff} increases at $\Delta T = 233$ °C, which we postulate is an effect of very fast clinopyroxene growth rates and strong disequilibrium uptake of incompatible cations into the crystal structure.

Model C: Machine learning thermobarometry

Finally, we test the machine learning random forest algorithm (Jorgenson *et al.*, 2022; 'Model C: Machine Learning'), which has uncertainties of ± 45 °C and ± 270 MPa (determined using a test data set) and was calculated using the python package Thermobar (Wieser *et al.*, 2022). Unlike Models A and B, $T_{measured}$ and $P_{measured}$ are not based off a single equation but rather calculated using a pool of experimental compositions that are constrained by specific $T_{measured}$ and $P_{measured}$. A key advantage of this approach is that a calibration data set that best fits the compositions of interest can be selected, and a confidence interval for each measurement can be assessed using the generated interquartile range (IQR). However, an inherent drawback of machine learning algorithms is that the exact parameters influencing P–T calculations are unknown. Importantly, unlike Models A and B, the machine learning approach is not based on a single thermodynamic model and may suffer from calibration overfitting (Wieser *et al.*, 2023a). Overall, our data return P–T estimates within the error of the calibration across ΔT conditions with no systematic overestimation or underestimation of P–T (Fig. 4, Supplementary Table 4). This suggests that this model may be suitable for a range of crystallisation conditions. Below, we explore results in detail and assess the uncertainty of our calculations following Jorgenson *et al.* (2022).

For 400 MPa experiments, $T_{calculated}$ are largely consistent with $T_{measured}$, resulting in a T_{diff} that lies within the uncertainty of the model with no systematic under or overestimation of T (Fig. 4). For example, as ΔT increases, T_{diff} in Al-poor zones has a maximum of 29 °C at $\Delta T = 132$ °C and is highest in Al-rich zones at $\Delta T = 25$ °C ($^{\text{Al-rich}}T_{diff} = 37$ °C). This is also reflected in the regression fits obtained for both T-induced and H_2O-induced ΔT, which both have $R^2 < 0.50$ (Supplementary Figure 4). This consistency across ΔT is also demonstrated by the weak correlation between T_{diff} and both clinopyroxene and melt compositions (as shown in correlation plots in Supplementary Figure 2). Although T_{diff} may not exceed the model uncertainty for our 400 MPa experiments, as outlined in Jorgenson *et al.* (2022), IQR can be used as an effective filter to assess the quality of calculated P and T. Overall, the IQR remains relatively unchanged with T_{diff} and ΔT. For $T_{calculated}$, the IQR of Al-poor zones is within the recommend limit for IQR values (Supplementary Figure 6). Al-rich zones are also typically within the limit, except for Al-rich prism sectors at $\Delta T = 32$ °C, which return an average IQR = 91 °C. On one hand, these results indicate that the machine learning model is less sensitive to kinetic effects related to ΔT, thus performing well for sector–zoned clinopyroxene crystals growing from mafic alkaline magmas. On the other hand, one of the shortfalls of the machine learning approach is the lack of empirical and thermodynamically-derived equations, making it difficult to determine the relative influence of clinopyroxene and melt components on the estimation of T crystallisation conditions.

Contrasting with the behaviour of T_{diff} with ΔT, P_{diff} exceeds the model uncertainty at high ΔT, mirroring the relationship observed for Model A (Fig. 4). For example, Al-poor and Al-rich zones always give conditions within the uncertainty range of Model C, except at high ΔT where clinopyroxene is dendritic ($^{\text{Al-poor}}P_{diff}$ increases from 48 to 310 MPa and $^{\text{Al-rich}}P_{diff}$ increases from 133 to 346 MPa as ΔT increases from 23 to173 °C). This reflects the strong influence of DiHd and Jd on P_{diff} (Supplementary Figure 2), where increasing Jd with ΔT causes greater deviations of $P_{calculated}$ from P_{known}. Considering the effects of T-induced and H_2O-induced ΔT separately, H_2O-induced ΔT has the largest influence on P_{diff} ($R^2 = 0.83$; Supplementary Figure 4), compared to T-induced ΔT ($R^2 = 0.40$). This mirrors the results from Models A and B, further emphasising that H_2O-induced ΔT is the most significant influence on the relative accuracy of $P_{calculated}$. As before, we also consider the recovered IQRs for each calculation of crystallisation pressure. On average, IQRs increase as ΔT increases from 23 to 173 °C for both Al-poor zones (IQR increases from 293 to 426 MPa) and Al-rich zones (IQR increases from 360 to 512 MPa; Supplementary Figure 6) but are typically within the limit of double the model uncertainty (540 MPa). However, although IQR remains within this limit, the calculated values typically correspond with those that deviate strongly from P_{known}, and hence this filter may not be useful in removing erroneous estimates of P.

For 800 MPa experiments, both T_{diff} and P_{diff} are relatively constant with increasing ΔT, except for $\Delta T = 133$ °C (Fig. 4). Indeed, correlation matrices highlight the poor correlation between T_{diff} and P_{diff} with clinopyroxene and melt components (Supplementary Figure 2). Al-poor zones have $T_{diff} = 40$ °C and $P_{diff} = 92$ MPa at $\Delta T = 83$ °C, decreasing slightly to $T_{diff} = 24$ °C and increasing to $P_{diff} = 117$ MPa at $\Delta T = 233$ °C. T_{diff} in Al-rich zones is also relatively unchanged with ΔT ($^{\text{Al-rich}}T_{diff}$ increases from 25 to 30 °C as ΔT increases from 83 to 233 °C). Similarly, P_{diff} of Al-rich zones is typically within the uncertainty range, particularly as ΔT increases ($^{\text{Al-rich}}P_{diff}$ decreases from 241 to 84 MPa at $\Delta T = 83$ and 233 °C, respectively). Comparing these results to IQR calculations, there appears to be no clear relationship between T_{diff}, P_{diff} and their respective IQR values, contrasting with the behaviour for P_{diff} at 400 MPa (Supplementary Figure 6). Combined with our results for 400 MPa experiments, this suggests that filtering results on the basis of IQR may not necessarily improve P–T results obtained by machine learning models, in agreement with the assessment of Wieser *et al.* (2023b).

Recommendations

Overall, our results indicate that different thermobarometric models may be suitable for different applications, depending on the nature of the original calibration data set. From our experimental results, we recommend the use of thermobarometers based on isothermal–isobaric experiments, such as Model A, to phenocrysts and microphenocrysts crystallising at low ΔT, including those that are sector-zoned. On the other hand, we propose that Model B, which also uses data from decompression experiments where clinopyroxene crystallises under variable ΔT, may be more appropriate to groundmass microlites and phenocryst rims (i.e., outermost rims) which formed during magma ascent and decompression. Machine learning approaches may be suitable for a range of crystallisation conditions and may provide a means to explore large data sets where textural conditions may not be well defined (e.g., crystal cores, sectors, and rims).

IMPLICATIONS FOR NATURAL CLINOPYROXENE

To test the equilibrium models and thermobarometers examined above, we used the compositions of sector-zoned clinopyroxene microphenocrysts and groundmass microlites from the 1974 eruption at Mt. Etna, described in Ubide *et al.* (2019). The microphenocrysts (200–500 μm width) exhibit composite zoning patterns (Fig. 5), consisting of; 1) partially resorbed cores which crystallised from pre-existing magma batches, 2) sector-zoned Cr-rich mantles formed upon mafic recharge and 3) Cr-poor rims (often referred to as 'outermost rims') formed during magma ascent and eruption (Ubide & Kamber, 2018; Ubide *et al.*, 2019; Mollo *et al.*, 2020; MacDonald *et al.*, 2022). We use major element data of these zones, in addition to groundmass microlites (Fig. 5), previously published in Ubide & Kamber (2018) and Ubide *et al.* (2019) and compiled in Supplementary Table 5. Using the classification scheme of Morimoto (1988), clinopyroxene microphenocrysts and microlites from the 1974 eruption classify as diopside–augite (Fig. 5).

The 1974 eruption at Mt. Etna was fed by deep, undegassed magmas bypassing the central conduits that feed summit eruptions and most flank eruptions, classifying as an eccentric eruption (Clocchiatti *et al.*, 2004; Métrich *et al.*, 2004; Corsaro *et al.*, 2009). Sector-zoned clinopyroxene crystals are common in eccentric eruptions (Magee *et al.*, 2021) and are defined by hourglass sectors {−1 1 1} enriched in Si + Mg and depleted in Al + Ti relative to prism sectors {*h k* 0}, interpreted to form under low ΔT growth conditions (Ubide *et al.*, 2019).

For the equilibrium melt composition, we use the bulk rock composition from a nearly aphyric sample from the 1974 eruption (160274FLA with <5 vol.% phenocrysts, Corsaro *et al.*, 2009).

Following our assessment of equilibrium models, we apply the DiHd, EnFs, CaTs and CaTi equilibrium models to our natural clinopyroxene data (Fig. 5; Supplementary Table 6). DiHd and EnFs both indicate equilibrium conditions for hourglass and prism sectors, with some core compositions excluded based on the DiHd equilibrium model (Fig. 5). These core compositions may have crystallised from more mafic melts with higher equilibrium DiHd compositions, typical of deep clinopyroxene crystallisation at Mt. Etna (e.g. Mollo *et al.*, 2020). As discussed previously, DiHd and EnFs components may be insensitive to sector-zoning (and ΔT), even when a single melt composition is used, due to the relatively fast diffusion of Ca and Mg in the melt. On the other hand, CaTs and CaTi are highly sensitive to ΔT and sector-zoning, as they are controlled by the incorporation of the slower diffusing Al and Ti into the crystal lattice, which is also strongly partitioned between sectors. Our results clearly indicate that filtering using CaTs and CaTi equilibrium models accounts for the effects of sector zoning; hourglass sectors have CaTs and CaTi compositions more closely aligned with equilibrium than prism sectors (Fig. 5). This illustrates that when using a single melt composition, equilibrium for slower diffusing species in the melt may not be achieved. Interestingly, ΔCaTi exhibits a V-shaped trend plotted against Mg#, where the trajectory of the trend differs based on the type of sector (negative for prism, positive for hourglass) and the merging point represents the compositions closest to equilibrium, which are those with lesser sector partitioning. In sector-zoned clinopyroxene from Stromboli volcano, Italy, a similar trend was observed for ΔDiHd (Scarlato *et al.*, 2021), and the authors determined the intermediate compositions (i.e. at the apex of the V shape) provide best *P–T* estimates, as these correspond to compositions fed by interface melts more closely approximated by the bulk melt composition used. Applied to our data, the vertex of the ΔCaTi and Mg# trend best approximates data within 2 SEE of equilibrium (Fig. 5). Groundmass microcrysts and microphenocryst rims yield equilibrium results comparable to prism sectors; DiHd and EnFs compositions are within the accepted limits of equilibrium, however some data points are too enriched in CaTs and CaTi for equilibrium with the bulk rock composition.

From our assessment of equilibrium models on experimental samples (Fig. 3), we filter the natural clinopyroxene–melt compositions using DiHd and EnFs to within 1SEE, and CaTs and CaTi to within 2SEE prior to calculation of *P–T* (Fig. 6). For comparison, we report thermobarometry results using just DiHd and EnFs filtering in Table 2. Overall, there is a striking difference in the *P–T* trend between Models A and B (with variations in pressure linked to those in temperature), and Model C, which suggests identical crystallisation *T* for all clinopyroxene zones (Fig. 6). Although the calculation of *T* using Model A is dependent on calculated *P*, this is not the case for Model B or Model C, and so it is unlikely that the interdependencies of *P* and *T* using a particular model are responsible for this observed trend. Instead, this may reflect a stronger sensitivity of thermometers A and B to clinopyroxene compositions, compared to Model C, where calculated *T* may be more exclusively influenced by melt composition (which we keep constant in our calculations). This trend may also be partly attributed to analytical uncertainty as suggested by Wieser *et al.* (2023a) and particularly emphasised for transcrustal storage trends like the ones we observe here.

We first consider *P–T* obtained from microphenocryst mantles and resorbed cores (Fig. 6, top panels). Broadly, crystallisation conditions recorded by prism and hourglass sectors in mantles are typically within the range of calibration uncertainty for a specific model but differ between models. For example, crystallisation *T* recorded by hourglass and prism sectors from Model A differs by 3 °C on average, which is well within the model uncertainty of ± 45 °C (Table 2). Results from Models B and C are also similar highlighting that when filtered based on our recommended series of equilibrium models (Fig. 5), hourglass and prism sectors give equivalent results for crystallisation *T*. For comparison, if clinopyroxene–melt compositions are filtered for equilibrium based only on the DiHd and EnFs models, the difference in recovered *T* is 13 °C for model A, and 27 °C for Model B (Table 2), demonstrating that using CaTs and CaTi models to filter for clinopyroxene–melt pairs results in a tighter estimate of *T* for sector-zoned crystals. In contrast, the difference in *T* between hourglass and prism sectors for Model C are not significantly affected by more rigorous clinopyroxene–melt equilibrium filtering.

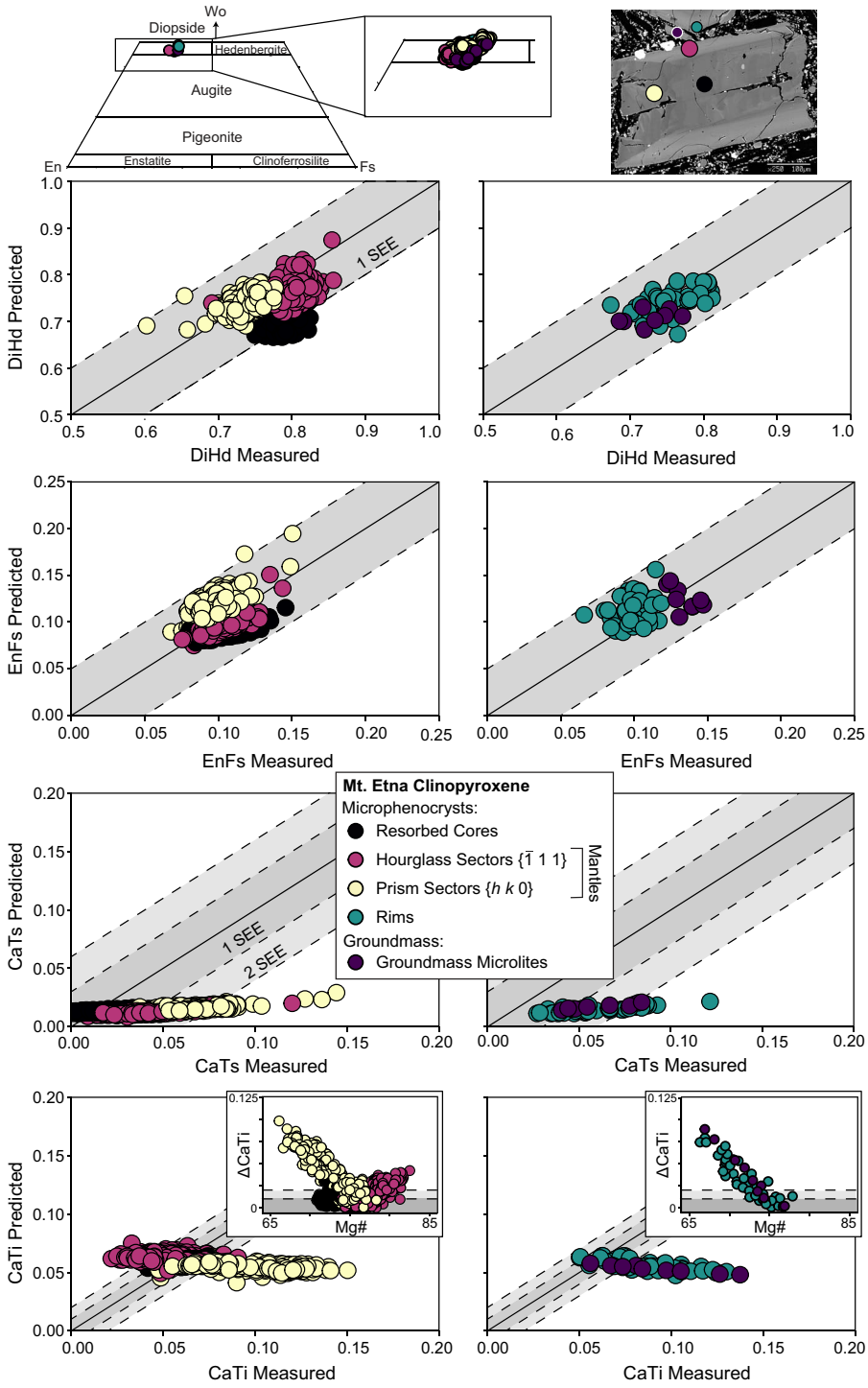

Fig. 5. Classification (top left), morphology (top right) and assessments of equilibrium of microphenocryst resorbed cores, sector-zoned mantles (left) and microphenocryst rims together with groundmass microlites (right) from the 1974 eccentric eruption, Mt. Etna (Italy). Data from Ubide & Kamber (2018) and Ubide *et al.* (2019). Accepted equilibrium ranges are shaded in grey and expanded to 2SEE for CaTs and CaTi considering the lower correlation between calibration data sets relative to 1SEE for DiHd and EnFs (Putirka, 1999). An insert of the relationship between ΔCaTi and Mg# is also included, illustrating the V-shaped relationship between the two parameters. Equilibrium is achieved at the apex of the V, corresponding to sector compositions fed by interface melts closely approximated by the bulk melt composition. The apex comprises both hourglass and prism sectors, highlighting the need to analyse and test for equilibrium using crystal faces parallel and perpendicular to the c crystallographic axis.

Regarding *P*, it is important to note that in mafic alkaline systems, such as Mt. Etna, where sector-zoning develops under low ΔT growth conditions, Na concentrations and hence the Jd component are not typically strongly partitioned between clinopyroxene sectors (Ubide *et al.*, 2019). This is unlike sector zoning in other alkaline settings where clinopyroxene textures indicate strong disequilibrium growth conditions such as spongy textures in Hawaiian ankaramites (Hammer *et al.*, 2016) and in tholeiitic settings such as Iceland, where Ca and Na show sector partitioning (e.g. Neave *et al.*, 2019). Therefore, we do not anticipate

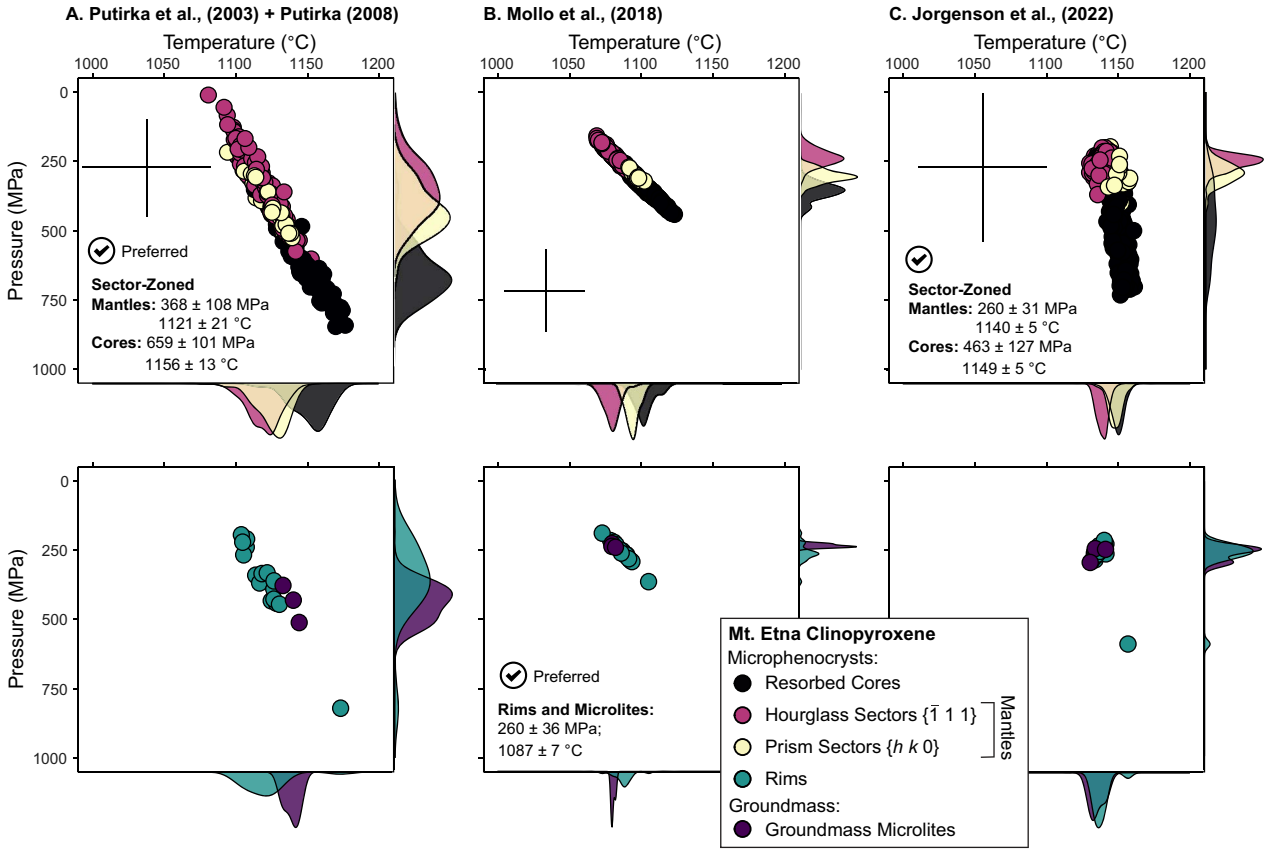

Fig. 6. Thermobarometry of clinopyroxene microphenocrysts (cores, sector-zoned mantles, and outermost rims) and groundmass microlites from the 1974 eccentric eruption. Only clinopyroxene–melt pairs that pass all DiHd, EnFs, CaTs and CaTi equilibrium models are presented here. Data are plotted in *P*–*T* diagrams, but also included as kernel density plots with bandwidths determined using the method of Scott (2015). Model uncertainties (based on calibration data sets for Models A and B, and a test data set for Model C) are represented in *P*–*T* diagrams by black crosses.

a significant difference between pressure conditions calculated from prism or hourglass sector compositions at Mt. Etna and other similar alkaline settings, as we observe in our results (Fig. 6; Table 2). Although compositions from prism sectors may on average be higher than those calculated using hourglass sectors (e.g. $P_{hourglass}$ = 355 MPa and P_{prism} = 398 MPa for Model A), values are within the range of uncertainty of the model and are therefore not large enough to be significant (Fig. 6). Like *T* estimates, the choice of equilibrium filtering impacts the divergence of estimates of crystallisation *P*, particularly for Models A and B (Table 2). The inclusion of CaTs and CaTi equilibrium models reduce the difference between $P_{hourglass}$ and P_{prism} by selecting only sectors that were in local equilibrium with an interface melt most similar in composition to the bulk melt, as discussed previously (Fig. 5). The difference in $P_{calculated}$ between sectors using Model C is relatively unaffected by the choice of equilibrium filtering, as observed for *T*. This suggests that machine learning approaches, may be well equipped to estimate crystallisation *P*–*T* from sector-zoned crystals regardless with limited constraints on equilibrium melt compositions.

Although all three thermobarometric models seem appropriate for application to sector zoned clinopyroxene in mafic alkaline systems, given that equilibrium is sufficiently accounted for, it is also useful to assess which of the three give *P*–*T* conditions that are consistent with crystallisation of clinopyroxene at Mt. Etna. During the 1974 eccentric eruption, Mt. Etna magma is considered to have risen rapidly from a depth of approximately 10 km (Corsaro *et al.*, 2009), which has also been identified using geophysical data as a region of magma storage (10 ± 3 km; Murru *et al.*, 1999). Using the crustal density model of Corsaro & Pompilio (2004), this corresponds to pressure conditions of 300–400 MPa. The growth of Cr-rich mantles in clinopyroxene crystals has been previously attributed to crystallisation within this region of magma storage (Ubide & Kamber, 2018). From our results, crystallisation pressures recorded by sector-zoned mantles are consistent with storage in this region and overlap with each other when uncertainties are accounted for (Table 2). We strongly emphasise that rather than assuming that only one sector is appropriate for thermobarometry, the priority should be placed on conducting a range of suitable equilibrium models to identify appropriate sectors. This is particularly important if a single melt composition is used, as the interface melt composition in local equilibrium with a particular sector may not be exactly equivalent to the bulk melt composition. We recommend using aphyric bulk rocks, groundmass or glass compositions as putative melts, to avoid crystal accumulation effects (Magee *et al.*, 2021, Ubide *et al.*, 2022, 2023).

In the resorbed cores, crystallisation temperature does not deviate significantly from those obtained from clinopyroxene mantles (Fig. 6; Table 2). In contrast, the difference between P_{cores} and $P_{mantles}$ is highly dependent on the thermobarometer used. Results from Model A indicate that resorbed cores crystallised at a pressure of 659 ± 101 MPa, deeper than the pressure predicted using Model C (463 ± 127 MPa) and Model B (355 ± 33 MPa; Table 2). Clinopyroxene crystallisation depths calculated using Model A are consistent with polybaric growth of clinopyroxene as frequently

Table 2: Average pressure (MPa) and temperature (°C) calculated from clinopyroxene microphenocryst cores, sector-zoned mantles and rims, and groundmass microlites from the 1974 eruption at Mt. Etna, Italy. Average *PT* for clinopyroxene–melt pairs that pass the DiHd, EnFs, CaTs and CaTi equilibrium models, and those that pass only DiHd and EnFs models are included. For the full data set, see Supplementary Table 5

Crystal	Zone	Sector	**DiHd*** + **EnFs*** + **CaTs^** + **CaTi^**						**DiHd*** + **EnFs***					
			Model A		Model B		Model C		Model A		Model B		Model C	
			T	*P*	*T*	*P*	*T*	*P*	*T*	*P*	*T*	*P*	*T*	*P*
Microphenocryst	Resorbed Core		1152 ± 13	659 ± 101	1104 ± 7	355± 33	1149 ± 5	463± 127	1152 ± 13	664± 101	1104± 7	356± 35	1149± 5	466± 125
	Mantle	Hourglass	1120 ± 11	355 ± 106	1081 ± 6	234± 30	1139 ± 4	254± 26	1118 ± 12	336± 111	1078± 7	222± 36	1139± 4	260± 28
		Prism	1123 ± 11	398 ± 103	1091 ± 8	278± 38	1143 ± 6	267± 44	1130 ± 12	461± 104	1105± 12	340± 56	1142± 6	285± 45
		Overall	1121 ± 16	368 ± 108	1084 ± 8	247± 39	1140 ± 5	260± 31	1125 ± 13	409± 124	1093± 17	289± 78	1140± 5	275± 34
	Rim		1121 ± 16	366 ± 143	1088 ± 7	263± 38	1138 ± 6	275± 84	1131 ± 17	450± 148	1101± 14	322± 67	1139± 5	301± 71
Groundmass microlite			1139 ± 6	442 ± 67	1081 ± 1	236± 7	1135 ± 5	263± 28	1145 ± 11	502± 113	1094± 16	295± 70	1137± 5	314± 52

*Values within 1 SEE of predicted ^Values within 2 SEE of predicted

described at Etna (e.g. Armienti *et al.*, 2007; Ubide & Kamber, 2018; Mollo *et al.*, 2020). This is not reflected in results obtained using Model B, which suggests low pressure crystallisation comparable to the mantles (Fig. 6; Table 2). However, as previously discussed, the calibration data set of Model B utilises decompression experiments which crystallised at low pressures (≤ 400 MPa) and underestimates crystallisation *P* at low ΔT (Fig. 4). Crystallisation pressures calculated using Model C indicate slightly deeper crystallisation than Model B, still shallower than Model A, but consistent with the main storage region at Mt. Etna (Murru *et al.*, 1999). Therefore, we prefer Model A or C to estimate core crystallisation conditions.

Microphenocryst rims and groundmass microlites at Mt. Etna are associated with shallow degassing and decompression phenomena (Ubide & Kamber, 2018), and typically incorporate higher concentrations of Al and Ti, consistent with growth under high ΔT (e.g. Masotta *et al.*, 2020). Interestingly, none of the three thermobarometers we assess give average crystallisation *P–T* distinct from those calculated for the clinopyroxene mantles using the same thermobarometer (Fig. 6, Table 2). As thermobarometry on clinopyroxene rims and microlites reflects the conditions at which clinopyroxene and melt were in equilibrium prior to ascent (e.g. Klügel *et al.*, 2015), and ascent during the 1974 eruption was rapid enough to preserve closed system dynamics (Corsaro *et al.*, 2009), it follows that these *P–T* conditions reflect the last event of clinopyroxene crystallisation prior to initial magma ascent (i.e. the kinetics of crystallisation were instantaneously frozen at the time of eruption). Considering the results from each thermobarometer, Model B gives the most invariant range of *P–T* conditions (260 ± 36 MPa and 1087 ± 7 °C), followed by Model C (273 ± 78 MPa and 1137 ± 6 °C) and Model A (347 ± 136 MPa and 1123 ± 16 °C). Trace element partitioning modelling reported in MacDonald *et al.* (2022) suggests growth of microphenocryst rims and groundmass microlites took place at $\Delta T > 55$ °C and 79 °C, respectively. This is consistent with the preferential use of Model B, which incorporates decompression and ΔT experiments and returns more accurate *P–T* at high ΔT in our experimental assessment (Fig. 4).

From our overall assessment of thermobarometric approaches, general overlap between hourglass and prism sectors across all three thermobarometric models highlights the need to carefully consider equilibrium testing for both sectors. We recommend using a combination of DiHd and EnFs models at 1 SEE (± 0.1 and ± 0.05, respectively; Mollo *et al.*, 2018) with CaTi and CaTs models at 2 SEE (± 0.06 and ± 0.02, respectively; Putirka, 1999), especially when using a single bulk melt composition which may not necessarily be identical to the local melt which fed the growth of each sector.

CONCLUSIONS

We investigate the effect of magma undercooling on the attainment of equilibrium between clinopyroxene and melt using a range of equilibrium models, and assess the influence of undercooling on the accuracy of thermobarometry. Our approach uses a set of experiments crystallised at variable undercooling conditions, where crystals ranged in morphology from polyhedral and sector-zoned with Al-rich prisms and Al-poor hourglass sectors to skeletal and dendritic with Al-rich skeletons and Al-poor overgrowths. We then test our insights on naturally occurring sector-zoned clinopyroxene microphenocrysts and microlites with well-constrained pre-eruptive histories. Our results show that:

- Equilibrium models that use the exchange of Fe–Mg between clinopyroxene and melt are insensitive to undercooling, and therefore of limited use when assessing clinopyroxene-melt equilibrium in sector-zoned crystals or microcrysts. The DiHd and EnFs equilibrium components indicate clinopyroxene-melt disequilibrium at high undercooling conditions ($\Delta T > 191$ °C). CaTs and CaTi models are more sensitive to undercooling and crystal zonation, and our experimental clinopyroxenes depart from equilibrium at $\Delta T > 25$ °C. We interpret this to reflect the slower diffusion of Al and Ti cations in the interface melt feeding crystal growth, hindering its equilibration with the far field melt. A combination of DiHd, EnFs, CaTs and CaTi is recommended to test for equilibrium between clinopyroxene and melt, as detailed below.
- Thermobarometers based on isothermal–isobaric experimental datasets (e.g. Putirka *et al.*, 2003; Putirka, 2008) are most accurate at low undercooling conditions, typical of magma stalling at depth and leading to the formation of crystal cores, whereas calibrations that expand their datasets to include decompression and undercooling experiments (Mollo *et al.*, 2018) are more reliable at higher degrees of undercooling, such as during magma decompression and degassing leading to growth of phenocryst rims and microcrysts. Machine learning approaches (e.g. Jorgenson *et al.*, 2022) are adaptable to the entire suite of undercooling conditions, but do not rely on a defined thermodynamic model. Undercooling induced by decreasing H_2O in the melt influences calculated pressure differently to undercooling induced by decreasing experimental resting temperature. For isothermal–isobaric thermobarometers, this implies that crystals grown under magma undercooling induced solely by cooling may provide more reliable estimates of pressure that those grown during decompression and degassing. In contrast, pressure estimates from thermobarometers, which include decompression experiments, may be more reliable if undercooling is related to degassing.
- Application of our experimental results to natural sector-zoned clinopyroxene microphenocrysts highlights that both hourglass and prism sectors are suitable for thermobarometry and selection of only one sector before analysis should be avoided. However, it is critical that clinopyroxene–melt pairs are screened using appropriate tests of equilibrium before the calculation of crystallisation pressure and temperature. We recommend the combination of four equilibrium models: DiHd (± 0.1), EnFs (1 SEE, ± 0.05), CaTs (2 SEE, ± 0.06) and CaTi (2 SEE, ± 0.02), when testing for equilibrium in sector-zoned clinopyroxene crystals, especially when using a single bulk melt composition. We suggest using 2 SEE for CaTs and CaTi equilibrium models to circumvent the larger spread in the original calibrations of these models, leading to looser correlations in the calibration dataset, and due to the slower diffusion of these components in the melt causing an interface melt that differs in composition from the far field melt under near-equilibrium growth conditions (i.e. sector zoning). We propose that this approach selects sectors closest to equilibrium with a bulk melt composition, reducing the difference between pressure and temperature estimates in hourglass and prism sectors, resulting in improved precision on pressure and temperature estimates for both sectors.
- The range of thermobarometry approaches we assess provide consistent *P–T* ranges for sector-zoned mantles in clinopyroxene microphenocrysts, highlighting that both traditional regression models and machine learning approaches can be used to estimate the crystallisation conditions of sector-zoned crystals. For resorbed cores, our results suggest that thermobarometers based on isothermal–isobaric experiments or machine learning approaches provide more realistic storage conditions. Conversely, models that also include decompression data are the best choice to reproduce *P–T* conditions of microphenocrysts outermost rims and groundmass microlites, recording the conditions at which clinopyroxene last equilibrated with the melt.

FUNDING

This work was supported by a Foundation Research Excellence Award from The University of Queensland and the Advance Queensland Women's Research Assistance Program from the Queensland Government to T.U. (UQ-FREA RM2019001828, WRAP109-2019RD1 RM2020002371). S.M., A.P. and M.M. benefited from the MIUR project 'Time scales of solidification in magmas: Applications to Volcanic Eruptions, Silicate Melts, Glasses, Glass-Ceramics' (PRIN 2017J277S9). A.M. was supported by the Australian Government Research Training Program (RTP; PhD scholarship) for the duration of this study. This publication includes work carried out at INGV-RM1 facilities with the support of EXCITE – EC- HORIZON 2020 -INFRAIA 2020 Integrating Activities for Starting Communities Trans-National Access action under grant agreement N.101005611.

DATA AVAILABILITY

The data used in this article are available in its online supplementary material.

ACKNOWLEDGMENTS

We acknowledge the facilities and staff of the Australian Microscopy and Microanalysis Research Facility at the Centre of Microscopy and Microanalysis (CMM), The University of Queensland. We would like to thank Manuela Nazzari for support with microprobe analysis at INGV, Rome, Al-Tamini Tapu for support with microprobe analysis at CMM, UQ and Olivier Higgins for discussion on machine learning approaches to clinopyroxene thermobarometry. We thank Penny Weiser, an anonymous reviewer and editorial handling by Madeleine Humphreys for their helpful comments that improved the manuscript.

References

Armienti, P., Tonarini, S., Innocenti, F. & Orazio, D. M. (2007). Mount Etna pyroxene as tracer of petrogenetic processes and dynamics of the feeding system. *Cenozoic Volcanism in the Mediterranean, Geological Society of America Special Papers* **418**, 265. https://doi.org/10.1130/2007.2418(13).

Blundy, J., Falloon, T., Wood, B. & Dalton, J. (1995). Sodium partitioning between clinopyroxene and silicate melts. *Journal of Geophysical Research: Solid Earth* **100**, 15501–15515. https://doi.org/10.1029/95JB00954.

Cashman, K. V., Sparks, R. S. J. & Blundy, J. D. (2017). Vertically extensive and unstable magmatic systems: a unified view of igneous processes. *Science* **355**, eaag3055. https://doi.org/10.1126/science.aag3055.

Clocchiatti, R., Condomines, M., Guénot, N. & Tanguy, J.-C. (2004). Magma changes at Mount Etna: the 2001 and 2002–2003 eruptions. *Earth and Planetary Science Letters* **226**, 397–414. https://doi.org/10.1016/j.epsl.2004.07.039.

Colle, F., Masotta, M., Costa, S., Mollo, S., Landi, P., Pontesilli, A., Peres, S. & Mancini, L. (2023). Effect of undercooling on clinopyroxene crystallization in a high K basalt: implications for magma dynamics at Stromboli volcano. *Lithos* **456-457**, 107327. https://doi.org/10.1016/j.lithos.2023.107327.

Corsaro, R. A. & Pompilio, M. (2004). Buoyancy-controlled eruption of magmas at Mt Etna. *Terra Nova* **16**, 16–22. https://doi.org/10.1046/j.1365-3121.2003.00520.x.

Corsaro, R., Métrich, N., Allard, P., Andronico, D., Miraglia, L. & Fourmentraux, C. (2009). The 1974 flank eruption of Mount Etna: an archetype for deep dike-fed eruptions at basaltic volcanoes and a milestone in Etna's recent history. *Journal of Geophysical Research: Solid Earth* **114**, B07204. https://doi.org/10.1029/2008JB006013.

Costa, F. (2021). Clocks in magmatic rocks. *Annual Review of Earth and Planetary Sciences* **49**, 231–252. https://doi.org/10.1146/annurev-earth-080320-060708.

Di Fiore, F., Mollo, S., Vona, A., MacDonald, A., Ubide, T., Nazzari, M., Romano, C. & Scarlato, P. (2021). Kinetic partitioning of major and trace cations between clinopyroxene and phonotephritic melt under convective stirring conditions: new insights into clinopyroxene sector zoning and concentric zoning. *Chemical Geology* **584**, 120531. https://doi.org/10.1016/j.chemgeo.2021.120531.

Downes, M. (1974). Sector and oscillatory zoning in calcic augites from M. Etna, Sicily. *Contributions to Mineralogy and Petrology* **47**, 187–196. https://doi.org/10.1007/BF00371538.

Dowty, E. (1976). Crystal structure and crystal growth: II. Sector zoning in minerals. *American Mineralogist* **61**, 460–469.

Dowty, E. (1980). Crystal growth and nucleation theory and the numerical simulation of igneous crystallization. In: Hargraves, R. (ed), *Physics of magmatic processes*. Princeton, NJ: Princeton University Press, 419–486, https://doi.org/10.1515/9781400854493.419.

Giacomoni, P. P., Ferlito, C., Coltorti, M., Bonadiman, C. & Lanzafame, G. (2014). Plagioclase as archive of magma ascent dynamics on "open conduit" volcanoes: the 2001–2006 eruptive period at Mt. Etna. *Earth-Science Reviews* **138**, 371–393. https://doi.org/10.1016/j.earscirev.2014.06.009.

Gualda, G. A., Ghiorso, M. S., Lemons, R. V. & Carley, T. L. (2012). Rhyolite-MELTS: a modified calibration of MELTS optimized for silica-rich, fluid-bearing magmatic systems. *Journal of Petrology* **53**, 875–890. https://doi.org/10.1093/petrology/egr080.

Hammer, J., Jacob, S., Welsch, B., Hellebrand, E. & Sinton, J. (2016). Clinopyroxene in postshield Haleakala ankaramite: 1. Efficacy of thermobarometry. *Contributions to Mineralogy and Petrology* **171**, 1–23.

Hollister, L. S. & Gancarz, A. J. (1971). Conpositional sextor-zoning in clinopyroxene from the narce area, Italy. *American Mineralogist: Journal of Earth and Planetary Materials* **56**, 959–979.

Iezzi, G., Mollo, S., Ventura, G., Cavallo, A. & Romano, C. (2008). Experimental solidification of anhydrous latitic and trachytic melts at different cooling rates: the role of nucleation kinetics. *Chemical Geology* **253**, 91–101. https://doi.org/10.1016/j.chemgeo.2008.04.008.

Iezzi, G., Mollo, S., Torresi, G., Ventura, G., Cavallo, A. & Scarlato, P. (2011). Experimental solidification of an andesitic melt by cooling. *Chemical Geology* **283**, 261–273. https://doi.org/10.1016/j.chemgeo.2011.01.024.

Jarosewich, E., Nelen, J. & Norberg, J. A. (1980). Reference samples for electron microprobe analysis. *Geostandards Newsletter* **4**, 43–47. https://doi.org/10.1111/j.1751-908X.1980.tb00273.x.

Jorgenson, C., Higgins, O., Petrelli, M., Bégué, F. & Caricchi, L. (2022). A machine learning based approach to clinopyroxene thermobarometry: model optimisation and distribution for use in earth sciences. *Journal of Geophysical Research: Solid Earth* **127**, e2021JB022904. https://doi.org/10.1029/2021JB022904.

Kirkpatrick, R. J. (1981) Kinetics of crystallization of igneous rocks. In: Lasaga, A. C., Kirkpatrick, R. J. (eds.), *Kinetics of geochemical processes*. Washington, DC: Mineralogical Society of America, pp. 321–398.

Klügel, A., Longpré, M.-A., García-Cañada, L. & Stix, J. (2015). Deep intrusions, lateral magma transport and related uplift at ocean island volcanoes. *Earth and Planetary Science Letters* **431**, 140–149. https://doi.org/10.1016/j.epsl.2015.09.031.

Kouchi, A., Sugawara, Y., Kashima, K. & Sunagawa, I. (1983). Laboratory growth of sector zoned clinopyroxenes in the system CaMgSi 2 O 6-CaTiAl 2 O 6. *Contributions to Mineralogy and Petrology* **83**, 177–184. https://doi.org/10.1007/BF00373091.

Leung, I. S. (1974). Sector-zoned titanaugites: morphology, crystal chemistry, and growth. *American Mineralogist: Journal of Earth and Planetary Materials* **59**, 127–138.

Longpré, M.-A., Klügel, A., Diehl, A. & Stix, J. (2014). Mixing in mantle magma reservoirs prior to and during the 2011–2012 eruption at El Hierro, Canary Islands. *Geology* **42**, 315–318. https://doi.org/10.1130/G35165.1.

MacDonald, A., Ubide, T., Mollo, S., Masotta, M. & Pontesilli, A. (2022). Trace element partitioning in zoned clinopyroxene as a proxy for undercooling: experimental constraints from trachybasaltic magmas. *Geochimica et Cosmochimica Acta* **336**, 249–268. https://doi.org/10.1016/j.gca.2022.09.007.

Magee, R., Ubide, T. & Caulfield, J. (2021). Days to weeks of syn-eruptive magma interaction: high-resolution geochemistry of the 2002-03 branched eruption at Mount Etna. *Earth and Planetary Science Letters* **565**, 116904. https://doi.org/10.1016/j.epsl.2021.116904.

Masotta, M., Freda, C., Paul, T. A., Moore, G. M., Gaeta, M., Scarlato, P. & Troll, V. R. (2012). Low pressure experiments in piston cylinder apparatus: calibration of newly designed 25 mm furnace assemblies to P= 150 MPa. *Chemical Geology* **312-313**, 74–79. https://doi.org/10.1016/j.chemgeo.2012.04.011.

Masotta, M., Pontesilli, A., Mollo, S., Armienti, P., Ubide, T., Nazzari, M. & Scarlato, P. (2020). The role of undercooling during clinopyroxene growth in trachybasaltic magmas: insights on magma decompression and cooling at Mt. Etna volcano. *Geochimica et Cosmochimica Acta* **268**, 258–276. https://doi.org/10.1016/j.gca.2019.10.009.

Métrich, N., Allard, P., Spilliaert, N., Andronico, D. & Burton, M. (2004). 2001 flank eruption of the alkali-and volatile-rich primitive basalt responsible for Mount Etna's evolution in the last three decades. *Earth and Planetary Science Letters* **228**, 1–17. https://doi.org/10.1016/j.epsl.2004.09.036.

Mollo, S., Del Gaudio, P., Ventura, G., Iezzi, G. & Scarlato, P. (2010). Dependence of clinopyroxene composition on cooling rate in basaltic magmas: implications for thermobarometry. *Lithos* **118**, 302–312. https://doi.org/10.1016/j.lithos.2010.05.006.

Mollo, S., Misiti, V., Scarlato, P. & Soligo, M. (2012). The role of cooling rate in the origin of high temperature phases at the chilled margin of magmatic intrusions. *Chemical Geology* **322-323**, 28–46. https://doi.org/10.1016/j.chemgeo.2012.05.029.

Mollo, S., Blundy, J., Iezzi, G., Scarlato, P. & Langone, A. (2013a). The partitioning of trace elements between clinopyroxene and trachybasaltic melt during rapid cooling and crystal growth. *Contributions to Mineralogy and Petrology* **166**, 1633–1654. https://doi.org/10.1007/s00410-013-0946-6.

Mollo, S., Putirka, K., Misiti, V., Soligo, M. & Scarlato, P. (2013b). A new test for equilibrium based on clinopyroxene–melt pairs: clues on the solidification temperatures of Etnean alkaline melts at

post-eruptive conditions. *Chemical Geology* **352**, 92–100. https://doi.org/10.1016/j.chemgeo.2013.05.026.

Mollo, S., Blundy, J., Scarlato, P., De Cristofaro, S. P., Tecchiato, V., Di Stefano, F., Vetere, F., Holtz, F. & Bachmann, O. (2018). An integrated PT-H2O-lattice strain model to quantify the role of clinopyroxene fractionation on REE+ Y and HFSE patterns of mafic alkaline magmas: application to eruptions at Mt. Etna. *Earth-Science Reviews* **185**, 32–56. https://doi.org/10.1016/j.earscirev.2018.05.014.

Mollo, S., Ubide, T., Di Stefano, F., Nazzari, M. & Scarlato, P. (2020). Polybaric/polythermal magma transport and trace element partitioning recorded in single crystals: a case study of a zoned clinopyroxene from Mt. Etna. *Lithos* **356-357**, 105382. https://doi.org/10.1016/j.lithos.2020.105382.

Morimoto, N. (1988). Nomenclature of pyroxenes. *Mineralogy and Petrology* **39**, 55–76. https://doi.org/10.1007/BF01226262.

Müller, T., Dohmen, R., Becker, H., Ter Heege, J. H. & Chakraborty, S. (2013). Fe–Mg interdiffusion rates in clinopyroxene: experimental data and implications for Fe–Mg exchange geothermometers. *Contributions to Mineralogy and Petrology* **166**, 1563–1576. https://doi.org/10.1007/s00410-013-0941-y.

Müntener, O., Kelemen, P. B. & Grove, T. L. (2001). The role of H 2 O during crystallization of primitive arc magmas under uppermost mantle conditions and genesis of igneous pyroxenites: an experimental study. *Contributions to Mineralogy and Petrology* **141**, 643–658. https://doi.org/10.1007/s004100100266.

Murru, M., Montuori, C., Wyss, M. & Privitera, E. (1999). The locations of magma chambers at Mt. Etna, Italy, mapped by b-values. *Geophysical Research Letters* **26**, 2553–2556. https://doi.org/10.1029/1999GL900568.

Nakamura, Y. (1973). Origin of sector-zoning of igneous clinopyroxenes. *American Mineralogist: Journal of Earth and Planetary Materials* **58**, 986–990.

Neave, D. A., Bali, E., Guðfinnsson, G. H., Halldórsson, S. A., Kahl, M., Schmidt, A.-S. & Holtz, F. (2019). Clinopyroxene–liquid equilibria and geothermobarometry in natural and experimental tholeiites: the 2014–2015 Holuhraun eruption, Iceland. *Journal of Petrology* **60**, 1653–1680. https://doi.org/10.1093/petrology/egz042.

Park, J., Lim, H., Myeong, B., Jang, Y.-D. & Brenna, M. (2022). Basaltic cognate enclaves from Dokdo Island as a window for intraplate mafic alkaline OIB magma dynamics in a back-arc basin. *Contributions to Mineralogy and Petrology* **177**, 1–23. https://doi.org/10.1007/s00410-022-01951-4.

Petrelli, M., Caricchi, L. & Perugini, D. (2020). Machine learning thermo-barometry: application to clinopyroxene-bearing magmas. *Journal of Geophysical Research: Solid Earth* **125**, e2020JB020130. https://doi.org/10.1029/2020JB020130.

Pontesilli, A., Masotta, M., Nazzari, M., Mollo, S., Armienti, P., Scarlato, P. & Brenna, M. (2019). Crystallization kinetics of clinopyroxene and titanomagnetite growing from a trachybasaltic melt: new insights from isothermal time-series experiments. *Chemical Geology* **510**, 113–129. https://doi.org/10.1016/j.chemgeo.2019.02.015.

Putirka, K. (1999). Clinopyroxene+ liquid equilibria to 100 kbar and 2450 K. *Contributions to Mineralogy and Petrology* **135**, 151–163. https://doi.org/10.1007/s004100050503.

Putirka, K. D. (2008). Thermometers and barometers for volcanic systems. *Reviews in Mineralogy and Geochemistry* **69**, 61–120. https://doi.org/10.2138/rmg.2008.69.3.

Putirka, K. D. (2017). Down the crater: where magmas are stored and why they erupt. *Elements* **13**, 11–16. https://doi.org/10.2113/gselements.13.1.11.

Putirka, K., Johnson, M., Kinzler, R., Longhi, J. & Walker, D. (1996). Thermobarometry of mafic igneous rocks based on clinopyroxene-liquid equilibria, 0–30 kbar. *Contributions to Mineralogy and Petrology* **123**, 92–108. https://doi.org/10.1007/s004100050145.

Putirka, K. D., Mikaelian, H., Ryerson, F. & Shaw, H. (2003). New clinopyroxene-liquid thermobarometers for mafic, evolved, and volatile-bearing lava compositions, with applications to lavas from Tibet and the Snake River Plain, Idaho. *American Mineralogist* **88**, 1542–1554. https://doi.org/10.2138/am-2003-1017.

Scarlato, P., Mollo, S., Petrone, C. M., Ubide, T. & Di Stefano, F. (2021). Interpreting magma dynamics through a statistically refined thermometer: implications for clinopyroxene Fe–Mg diffusion modeling and sector zoning at stromboli. *Crustal magmatic system evolution: anatomy, architecture, and physico-chemical processes* , 195–212. https://doi.org/10.1002/9781119564485.ch9.

Scott, D. W. (2015) *Multivariate density estimation: theory, practice, and visualization*. John Wiley & Sons.

Shea, T. & Hammer, J. E. (2013). Kinetics of cooling-and decompression-induced crystallization in hydrous mafic-intermediate magmas. *Journal of Volcanology and Geothermal Research* **260**, 127–145. https://doi.org/10.1016/j.jvolgeores.2013.04.018.

Tanguy, J.-C., Condomines, M. & Kieffer, G. (1997). Evolution of the Mount Etna magma: constraints on the present feeding system and eruptive mechanism. *Journal of Volcanology and Geothermal Research* **75**, 221–250. https://doi.org/10.1016/S0377-0273(96)00065-0.

Ubide, T. & Kamber, B. S. (2018). Volcanic crystals as time capsules of eruption history. *Nature Communications* **9**, 326–312. https://doi.org/10.1038/s41467-017-02274-w.

Ubide, T., Márquez, Á., Ancochea, E., Huertas, M. J., Herrera, R., Coello-Bravo, J. J., Sanz-Mangas, D., Mulder, J., MacDonald, A. & Galindo, I. (2023). Discrete magma injections drive the 2021 La Palma eruption. *Science Advances* 9.

Ubide, T., Mollo, S., Zhao, J.-X., Nazzari, M. & Scarlato, P. (2019). Sector-zoned clinopyroxene as a recorder of magma history, eruption triggers, and ascent rates. *Geochimica et Cosmochimica Acta* **251**, 265–283. https://doi.org/10.1016/j.gca.2019.02.021.

Ubide, T., Neave, D. A., Petrelli, M. & Longpré, M.-A. (2021). Crystal archives of magmatic processes. *Frontiers in Earth Science* **9**. https://doi.org/10.3389/feart.2021.749100.

Ubide, T., Larrea, P., Becerril, L. & Galé, C. (2022). Volcanic plumbing filters on ocean-island basalt geochemistry. *Geology* **50**, 26–31. https://doi.org/10.1130/G49224.1.

Wieser, P., Petrelli, M., Lubbers, J., Wieser, E., Kent, A. J. & Till, C. (2022). Thermobar: an open-source Python3 tool for thermobarometry and hygrometry. *Volcanica* **5**, 349–384. https://doi.org/10.30909/vol.05.02.349384.

Wieser, P. E., Kent, A. J. R., Till, C. B., Donovan, J., Neave, D. A., Blatter, D. L. & Krawczynski, M. J. (2023a). Barometers behaving badly I: assessing the influence of analytical and experimental uncertainty on clinopyroxene thermobarometry calculations at crustal conditions. *Journal of Petrology* **64**. https://doi.org/10.1093/petrology/egac126.

Wieser, P. E., Kent, A. J. & Till, C. B. (2023b). Barometers behaving badly II: a critical evaluation of Cpx-only and Cpx-Liq thermobarometry in variably-hydrous arc magmas. *Journal of Petrology* **64**. https://doi.org/10.1093/petrology/egad050.

Zhang, Y., Ni, H. & Chen, Y. (2010). Diffusion data in silicate melts. *Reviews in Mineralogy and Geochemistry* **72**, 311–408. https://doi.org/10.2138/rmg.2010.72.8.

Zhou, J.-S., Wang, Q., Xing, C.-M., Ma, L., Hao, L.-L., Li, Q.-W., Wang, Z.-L. & Huang, T.-Y. (2021). Crystal growth of clinopyroxene in mafic alkaline magmas. *Earth and Planetary Science Letters* **568**, 117005. https://doi.org/10.1016/j.epsl.2021.117005.